Multipair phase-modulated temporal interference electrical stimulation combined with fMRI.

Iurii Savvateev[1], Florian Missey[2], Valeriia Beliaeva [1], Marija Markicevic[3], Diana Kindler[4,5], Daniel Razansky[4,5], Viktor Jirsa[6], Adam Williamson[2,6†], Rafael Polania[1†,] and Valerio Zerbi[7,8†]

[1] Decision Neuroscience lab, Department of Health Sciences and Technology, ETH Zurich, Switzerland
[2] International Clinical Research Center, St. Anne's University Hospital Brno, Brno, Czech Republic
[3] Department of Radiology and Biomedical Imaging, Yale School of Medicine, United States
[4] Institute of Pharmacology and Toxicology and Institute for Biomedical Engineering, Faculty of Medicine, University of Zurich, Switzerland
[5] Institute for Biomedical Engineering, Department of Information Technology and Electrical Engineering, ETH Zurich, Switzerland
[6] Aix-Marseille Université, Inserm, Institut de Neurosciences des Systèmes (INS) UMR_S 1106, Marseille, France
[7] Neuro-X Institute, School of Engineering (STI), EPFL, Lausanne, Switzerland
[8] CIBM Centre for Biomedical Imaging, Lausanne, Switzerland

[†] Shared last authorship

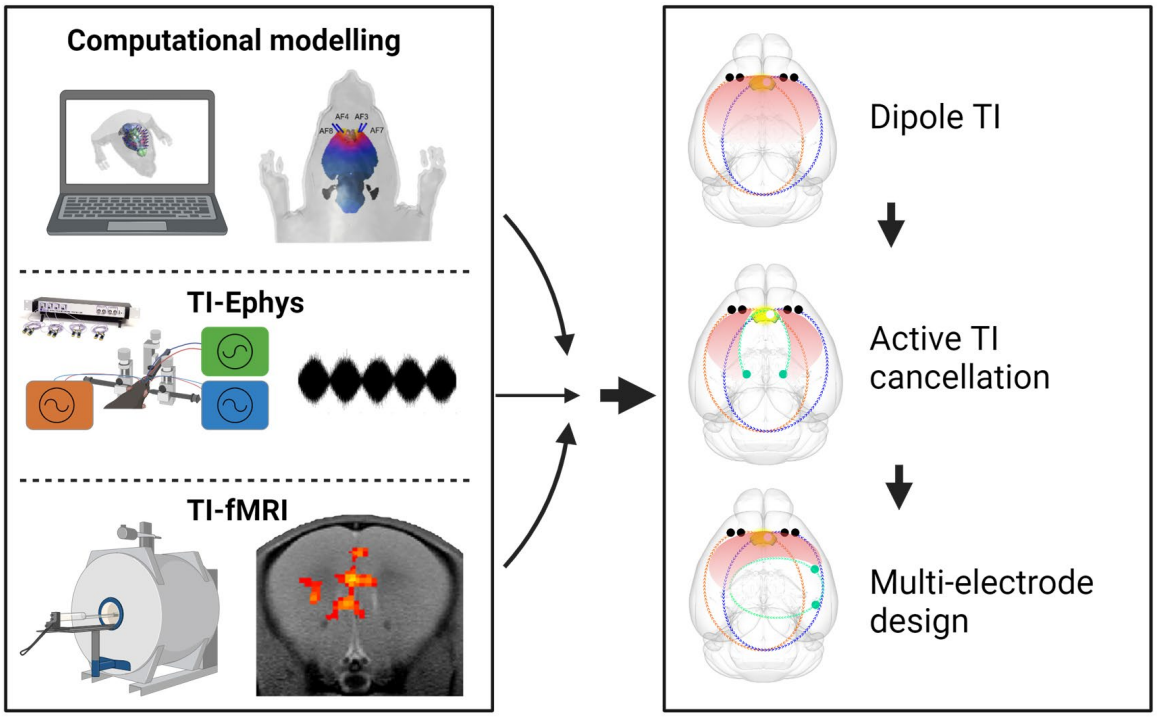

Abstract

Temporal Interference Stimulation (TI) is a novel brain stimulation technique that aims to integrate the depth characteristic of conventional deep brain stimulation protocols with the non-invasive nature of transcranial electric stimulation. Recent publications in both mice and humans demonstrate that subcortical areas including hippocampus and striatum can be targeted using TI. However, whereas TI stimulation is set to be focused on a specific region of interest, other off-target areas may still be stimulated, including cortical structures. This is a major concern as off-target stimulation carries the risk of modulating unwanted brain structures and circuits. In the present study, we focused on the prefrontal cortex (PFC) in mice and developed a computational modelling approach to identify the best electrode locations for targeting PFC. Using *in-vivo* electrophysiological recordings and functional magnetic resonance imaging (fMRI) combined with TI, we confirmed the presence of induced TI fields and hemodynamic responses in the PFC but also identified off-target stimulated sites. To minimize the occurrence of off-target effects, we propose a new configuration with three electrode pairs, one of which has an active phase shift of 180 degrees in relation to the other two TI-inducing pairs. The use of this phase-canceling field allowed us to improve the focality of TI by reducing off-target stimulations without significantly affecting the TI field in the target area. The proposed design effectively addresses one of TI's most critical shortcomings and opens new avenues for applications.

Introduction

Our understanding of the interplay between the brain and behavior has been significantly advanced by the utilization of non-invasive brain stimulation approaches. These techniques offer a non-intrusive and secure means to modulate neural processes in the healthy brain, thereby allowing researchers to directly investigate how experimentally manipulated neural activity causally influences behavior. This distinctive feature of non-invasive brain stimulation methods has, on one hand, yielded groundbreaking insights into the neurological foundations of various aspects of behavior alongside its potential clinical and practical applications (Beliaeva, Savvateev, Zerbi, & Polania, 2021).

One such non-invasive brain stimulation approach is transcranial electrical stimulation, which harnesses electrical currents applied to the scalp in the order of a few milliamperes (e.g., intensities of about 0.5-4 mA), intending to modulate neural activity and their corresponding neurocognitive functions in a relatively focal manner. The degree of invasiveness and the focality of the delivered stimulation are two key factors that distinguish between non-invasive (Alexander et al., 2019; Frohlich & Riddle, 2021; Grover, Nguyen, Viswanathan, & Reinhart, 2021; Zandvakili, Berlow, Carpenter, & Philip, 2019) and invasive (Sullivan, Olsen, & Widge, 2021; Williams et al., 2018) stimulations.

Non-invasive brain stimulation, such as transcranial magnetic stimulation (TMS) and transcranial direct (Zandvakili et al., 2019) or alternating (Alexander et al., 2019; Frohlich & Riddle, 2021; Grover et al., 2021) current stimulations (tDCS and tACS), gained increasing popularity in recent years due to their great potential in treating various psychiatric disorders such as depression spectrum (Alexander et al., 2019; Frohlich & Riddle, 2021; Sullivan et al., 2021; Williams et al., 2018; Zandvakili et al., 2019) and OCD (Grover et al., 2021). However, transcranial stimulation methodologies are typically utilized to selectively affect cortical structures owing to their limited depth penetration (Voroslakos et al., 2018).

Invasive brain stimulation techniques, such as deep brain stimulation (DBS) (Sullivan et al., 2021), involve the placement of electrodes into the brain. Kindled by the therapeutic usage of DBS in Parkinson patients at the second half of 20th century (Oliveria, 2018), DBS is currently expanded to the treatment of various psychiatric and neurodegenerative disorders such as: OCD, depression, addiction, Tourette and Parkison Disease (Dandekar, Fenoy,

Carvalho, Soares, & Quevedo, 2018; Krack, Hariz, Baunez, Guridi, & Obese, 2010; Mayberg et al., 2005). Invasive brain stimulation techniques, such as DBS, are more precise and effective in targeting specific brain regions and circuits but carry a higher risk of complications, such as infection, bleeding, and damage to surrounding brain tissue (Ramirez-Zamora et al., 2018).

Hence, the clinical indication between invasive and non-invasive techniques depends on the specific needs of the patient and the condition being treated. In some cases, non-invasive techniques may be sufficient to achieve the desired therapeutic effect, while in other cases, invasive techniques may be necessary to achieve the required precision and effectiveness.

In recent years, a non-invasive brain stimulation protocol called temporal interference stimulation (TI) was developed, permitting the stimulation of subcortical structures, for instance the hippocampus, without entraining the activity of the overlying cortex (Grossman et al., 2017). TI relies on the use of topical electrodes, placed directly on a scalp. In the case of a dipolar TI, two electric fields are delivered through these electrodes. The waveform of the electric fields and their amplitude can be selected on demand as soon as the frequency of these carrier's field is higher than 1 kHz ($f2 > f1 > 1000$ Hz). As the waves travel in the brain, they overlap and interfere in a desired region in which the destructive and additive interference of the stimuli will create an envelope frequency in the Hz range ($\Delta f = f2 - f1$). This envelope oscillation at Hz range is suggested to affect the neurons resting membrane potential, whereas frequencies in the kHz are suggested to have no effect on neural activity (Grossman et al., 2017)(but see (Budde, Williams, & Irazoqui, 2023; Mirzakhalili, Barra, Capogrosso, & Lempka, 2020) arguing against this explanation of the TI mechanism).

During the last years a number of studies in mice and humans demonstrated the utility of TI for stimulating deep brain areas, such as hippocampus (Acerbo et al., 2022; Missey et al., 2022; Missey et al., 2021), superior colliculus (Botzanowski et al., 2023; S. X. Song, Zhang, Tian, Wang, & Wei, 2021) and striatum (Wessel et al., 2021), as well as non-brain structures such as sciatic nerve (Botzanowski et al., 2022; Budde et al., 2023; Missey et al., 2023) and bladder (J. Lee et al., 2021). Despite the success of these applications, a computational modelling study by (Mirzakhalili et al., 2020) conducted in-depth analysis of the TI biophysics and suggested the presence of potential off-target TI stimulations when stimulating neurons. The *in-silico* prediction of off-target TI stimulations was later supported by *in-vivo* data from Missey and colleagues, who found that upon an increase of TI amplitude to target the CA3 area of the

mouse hippocampus, the off-target TI envelope in the neighboring motor cortex became powerful enough to cause arbitrary motor behaviors and, at high enough amplitudes (1.5 mA), convulsions (Missey et al., 2021). At the same time, Acerbo et al. explicitly measured Local Field Potentials (LFP) while doing TI stimulation of anterior hippocampus in human cadavers and reported the off-target TI envelope in the central hippocampus and at the overlaying cortex (Acerbo et al., 2022).

Other approaches that aim to enhance the focality of transcranial induction (TI) using supplementary electric fields, such as multipair TI, have been suggested. However, these proposals have primarily emanated from computational investigations (Cao & Grover, 2020; X. Song, Zhao, Li, Liu, & Ming, 2021) or examinations of peripheral nerves (Budde et al., 2023; Goats, 1990), thus lacking empirical validation when applied to brain structures (with the exception for (Botzanowski et al., 2023)). In the present study, we conducted a series of computational optimization procedures and empirical studies with the objective of identifying an optimal dipole configuration for inducing stimulation in the mouse medial prefrontal cortex (mPFC), a brain structure associated with the processing of reward-related information and the application of reward-seeking strategies (Padoa-Schioppa & Assad, 2006).

We validate the feasibility of TI *in vivo*, while concurrently quantifying the presence of residual TI stimulation in neighbouring off-target regions through electrophysiological recordings (Ephys) in selected regions of interest. Additionally, we introduce an innovative strategy for observing TI-related hemodynamic responses across the entire brain using functional MRI (fMRI). An additional contribution of our work is the development of a novel TI design featuring a cancellation field that exhibits an active phase shift of 180 degrees relative to the dipole fields, aimed at mitigating off-target effects associated with dipole stimulation. Our findings, based on both theoretical modelling and empirical evidence, establish that the incorporation of an additional phase-shifted cancellation field can significantly enhance the spatial precision of dipole TI stimulation. This improvement is achieved by minimizing off-target stimulatory effects, while concurrently preserving the integrity of the TI field within the intended cortical area. The innovative design introduced in this study effectively addresses a fundamental limitation of TI, thus opening new possibilities within the realm of its applications.

Results

Temporal interference (TI) stimulation with dipole configuration

Optimal electrode placement with mathematical modelling.

To determine an optimal electrode configuration for targeting the prefrontal cortex using temporal interference stimulation (TI), a modeling pipeline was devised to assess the efficacy of TI under various experimental setups. The pipeline consisted of three stages, namely (i) the construction of a head model with electrodes, (ii) the simulation of the electric fields, (iii) and the comparison of the resulting TI fields. The pipeline was implemented using Sim4Life, a simulation platform developed by Zurich Med Tech AG, Switzerland.

We first sought to establish an optimal configuration for positioning two electrode pairs (i.e. dipole stimulation). The coordinates of our target ROI were based on Allen Brain Common Coordinate Framework (ccv3) and centered on the right infralimbic cortex (IL) (Wang et al., 2020). Using Sim4Life software (Zurich Med Tech AG, Switzerland), we simulated TI fields within the mouse brain under different placements for the dipole on the scalp. Overall, 38 electrodes were placed according to high-density EEG system to be tested as potential stimulation or ground electrodes (M. Lee, Kim, Shin, Sung, & Choi, 2011) (Fig 1A). To assess the efficacy of these TI fields for targeting the IL, two parameters were computed for each stimulation: threshold and focality. The threshold corresponded to the median TI field calculated within the IL, whereas the focality was calculated as the ratio between the volume activated higher than the threshold in the IL and the whole brain. Finally, a database containing threshold and focality values for each simulated TI field was created. The TI field with the highest focality was chosen as the optimal one (Fig 1B). We identified the TI fields generated using two electrode pairs placed on EEG positions AF3/AF7 and AF4/AF8 (as depicted in Figure 1B), as the optimal.

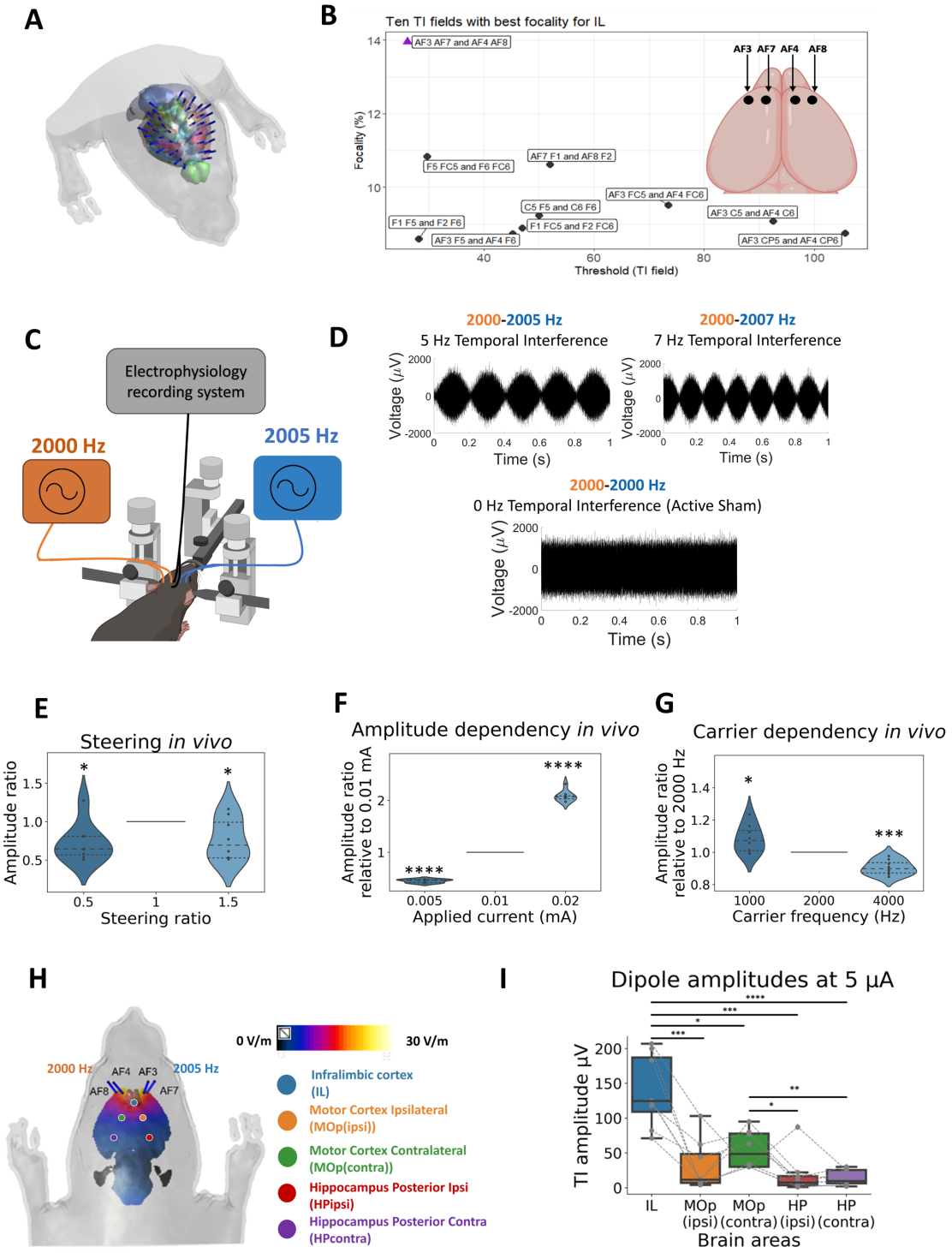

Figure 1. Limited TI dipole focality

A: Highly segmented mouse model with physiologically possible positions of stimulation electrodes positioned on the head skin **B:** Ten electrode configurations with the best focality values for the stimulation of the IL area. The TI field generated with AF3, AF7 and AF4, AF8 electrode configuration had the highest focality. **C:** Experimental setup for the dipole stimulation. Blue and Orange boxes depict independent current sources generating AC with the frequencies of 2000 and 2005 Hz, Grey box features electrophysiology recording system (see Methods for details) **D:** Raw data examples of the

envelope modulation (5 and 7Hz) and Active Sham recorded in IL. **E:** Steering of TI amplitude outside of IL **F:** Scaling of TI amplitude in IL by changing currents applied to the stimulators **G:** Dependence of TI amplitude in IL from the carrier frequency **H:** Location of stimulation (dark blue) and all recording (light blue, yellow, green, purple, red) electrodes superimposed on the model prediction of TI field (heatmap). IL target is highlighted in light pink on the heatmap **I:** Average TI amplitudes at the recorded brain areas (n=8) with the color matching H, p-values are FDR corrected. *p<0.05, **p<0.01, ***p<0.001, ****p<0.0001. ns-nonsignificant,

Studying of TI stimulation focality assessment with Electrophysiology

To measure the induction of TI stimulation in and outside of the target region (IL) for above-described dipole configuration we performed LFP recordings in anesthetized mice (Fig 1C). We measured TI induction in four brain regions, including proximal (primary motor cortex (MOp)) and distal (hippocampus (HP)) regions to the IL. For TI stimulation, we applied 5 µA alternating current (AC) to each of two independent current sources producing sine waves at either 2000 or 2005 Hz, thereby inducing an amplitude modulation at the frequency of 5 Hz (Fig 1D).

Firstly, we focused on the LFPs recorded from IL area. Similarly to (Grossman et al., 2017) we showed both *in-vivo* and *ex-vivo* that the frequency of the amplitude modulation (i.e TI stimulation) is determined by a difference in the frequencies between TI inducing fields and that Active Sham stimulation does not induce any amplitude modulation (Fig 1D, Fig S1A). Through the manipulation of current ratios between the TI inducing fields, we could further demonstrate an active modulation of TI amplitudes (i.e steering). Steering can efficiently, and on-demand adjust the stimulation target, without repositioning the topical electrodes. Our initial hypothesis posited a reduction in TI amplitude when utilizing unequal current ratios, as the positioning of the stimulation electrodes had been optimized to target the IL isocenter (AP: +1.54, ML: 0, DV: -2.8) through the application of equal currents. Our experimental findings, both *in-vivo* and *ex-vivo*, validated this assumption by demonstrating a decrease in TI amplitude for both the 0.5:1 and 1:1.5 steering ratios (see Fig 1E and Fig S1B). Furthermore, our investigations revealed a direct proportionality between TI amplitude and the amplitudes of the applied high-frequency fields, such as 2000 or 2005 Hz (see Fig 1F and Fig S1D). Conversely, TI amplitude displayed an inverse relationship with the carrier frequency of the fields (see Fig 1G and Fig S1C).

Secondly, we compared TI amplitude in IL, MOp (MOp_{ipsi}/MOp_{contra}: ipsilateral/contralateral to the recorded IL site) and HP (HP_{ipsi}/HP_{contra}: ipsilateral/contralateral to the recorded IL site). As predicted by the computational model (Fig 1H), the TI amplitude in IL was the highest compared to other recorded areas and decreased along AP axis (Fig 1I). Nevertheless, the distributions of TI amplitudes in MOp and HP were significantly higher than Active Sham (MOp(ipsi): W(8)=0, p=0.008, MOp(contra): W(8)=0, p=0.008, HP(ipsi): W(8)=0, p=0.008, HP(contra): W(7)=0, p=0.008) indicating a passive induction of TI in these areas. To ensure that detected TI in MC and HIP does not result from the propagation of TI from IL through the conductive brain tissue (e.g. axonal projections), we measured phases of TI oscillations at MC and HIP relative to IL (Table S1). The detected phase shifts were clustered at 0, 180, 360 degrees, suggesting that the corresponding TI in these areas happened due to passive induction (i.e. volume conduction) (Cohen, 2015). This experiment demonstrated that by using a dipole arrangement, we can induce TI stimulation in the IL region. TI was, however, passively induced in distant and off-target brain areas. Even with optimal electrode placements and current ratios, we showed that passive TI stimulation is diminished but not abolished by reducing the amplitudes of TI-inducing fields.

TI stimulation of IL with tripole configuration

The cumulative findings from our dipole TI stimulation underscore the imperative for continued refinement in achieving enhanced focal precision. To do that, we decided to introduce an additional pair of electrodes that would produce a field 180 degrees shifted with respect to the stimulation fields of our original dipole configuration (antiphase field). We argue that employing an active phase shift - a phase shift produced by the function generator - and an anatomy driven position of the cancellation pair, one may increase the focality of TI without requiring symmetrical electrode placement, and potentially minimizing the number of electrodes compared to previous multipair TI designs (Botzanowski et al., 2023; Budde et al., 2023; Cao & Grover, 2020; Goats, 1990; X. Song et al., 2021).

Cancellation of TI stimulation with an antiphase field

To validate empirically the mathematical demonstration of field-cancellation, we chose IL as a target brain region as to both inducing and cancelling TI fields (front tripole stimulation). The cancelling field was generated by introducing an additional independent current source with the same frequency as one of the stimulation fields (i.e., 2000Hz), but phase-shifted of 180 degrees compared to both stimulation fields (i.e., 2000 and 2005Hz) (Fig 2A). Using COMSOL © software we computed TI field (e.g., *in-silico*) in the IL area with different amplitudes of the cancelling field (cancelling weights). To confirm the validity of our modeling outcomes, we conducted experimental measurements of LFPs in anesthetized mice while applying different cancelling weights.

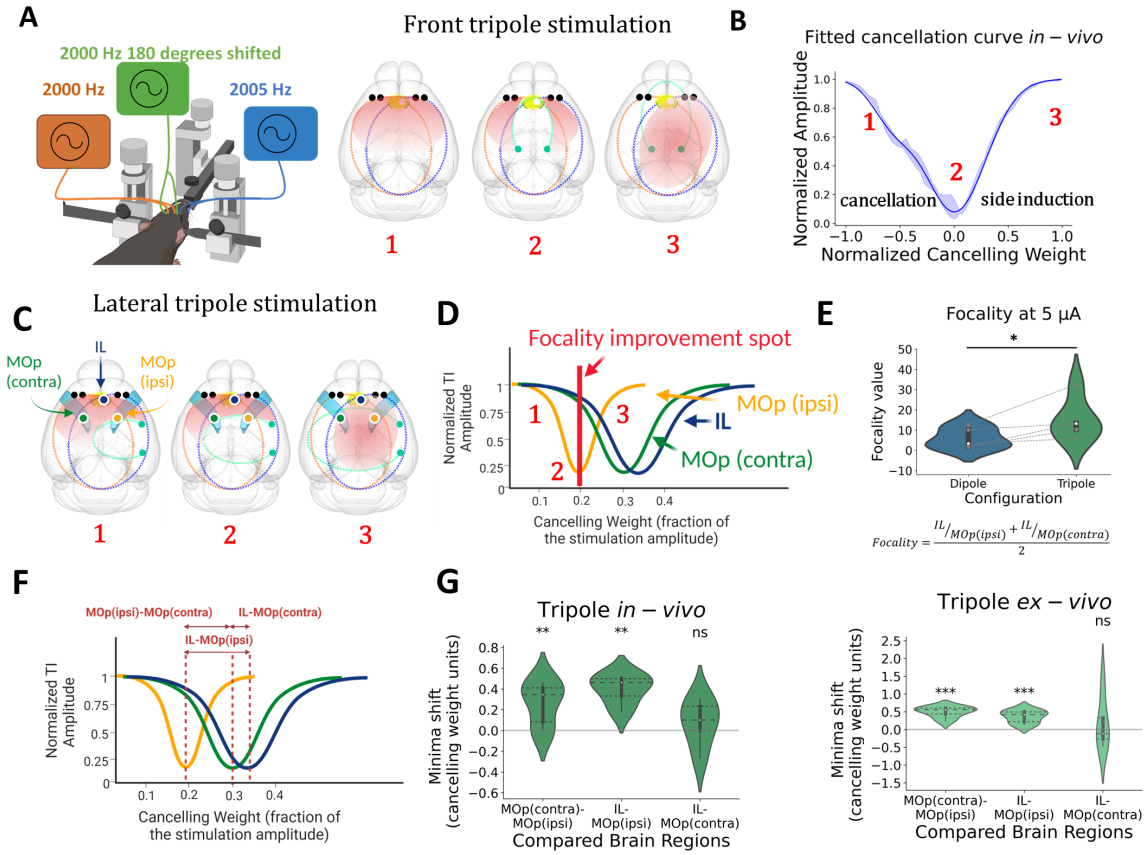

Figure 2. Enhancing focality through tripole configuration in brain stimulation

A: Experimental design for tripole stimulation and suggested TI field location (red) for each stage (1-3) of the cancellation process (colors of stimulators match the field lines). **B:** TI amplitude in IL at different cancelling weights in *in-vivo* front tripole stimulation experiments (n=9), solid line represents the fitted model at a group level and shaded area depicts bootstrapped confidence interval (Q1 and Q3 percentiles). **C:** Electrode configuration (black and green) and suggested TI field location (red) for each stage (1-3) of the cancellation in lateral tripole stimulation experiment. **D:** Proposed cancellation scheme for each of the recorded regions (colors match A) and a suggested focality improvement spot (red line). **E**: Comparison of the focality values with and without cancellation field. **F:** Scheme of the minima shift analysis **G:** Minima shifts between the cancellation curves from IL and MOp for the *in-vivo* and *ex-vivo* setups, p-values are FDR corrected. *p<0.05, **p<0.01, ***p<0.001. ns-nonsignificant.

A stepwise increase of the canceling weight led to a cancellation curve in IL in both *in-silico* and *in-vivo* setups (Fig 2B, Fig S2). We explained the obtained cancellation curve as the result of two co-occurring processes: “cancellation” and “side induction” (Fig 2A 1 and 3). *Cancellation* refers to the destruction of the temporal interference by a canceling field (stages “1” and “2” in Fig 2A), whereas side induction attributes to temporal interference occurring between the cancellation field and one of the stimulation fields (stage “3” in Fig 2A). Specifically, side induction occurs between a cancellation field (e.g. 180 degrees shifted 2000 Hz, Green in Fig 2A) and a stimulation field with which the cancellation field has a shift in the frequency (e.g. 2005 Hz, Blue in Fig 2A). Upon an initial increase of the cancelling weight, TI amplitude in IL decreased due to cancellation (Fig 2A, 1, and 2). However, with a further increase of the canceling weight, a larger portion of the cancellation field interfered with one of the stimulation fields, therefore, boosting side induction. The increase in side induction ultimately caused an increase in the TI amplitude in IL (Fig 2A 3). The cancellation curve was symmetrical with respect to the minimum TI amplitude and was well-fitted with a double Gaussian curve at the group level (Fig 2B) and in individual animals *in-vivo* (Fig S2). The symmetry of the cancellation curve suggests that the processes driving the results on either side of the curve are similar, further validating the mechanism of cancellation we proposed above. We also noted analogous symmetrical cancellation curves in *ex-vivo* experiments with transcranial electrode positioning (Fig S4). These curves exhibited compatibility with the same category of double Gaussian curves. In addition to describing the active-phase cancellation for Temporal Interference stimulation we showed that the same principle can be translated for Hz oscillations typical to tACS (Fig S3), allowing an additional mode of amplitude modulation (AM) for tACS (for the review of the current AM-tACS, see (Wu, Liu, & Wang, 2021).

Improving the focality of TI stimulation with a cancelling field

Having established the susceptibility of dipole TI fields to disruption through the introduction of a third, 180-degree-shifted field, we proceeded to investigate the potential of a cancellation field in averting TI induction in non-targeted regions and enhancing focality. In pursuit of this objective, we employed the dipole design as previously described for inducing TI in the IL and introduced a set of cancellation electrodes to effectively eliminate residual TI in MOp(ipsi) (Fig 2C).

As previously demonstrated, the process of TI field cancellation in each specific brain region is delineated by a cancellation curve. Employing this understanding, we strategically positioned a cancellation field in proximity to the region where off-target TI had been identified, specifically MOp(ipsi), and meticulously adjusted the cancellation amplitude to attain the minimum TI value within MOp(ipsi) (FIg 2D). This method allowed us to reduce the off-target TI envelope in MOp(ipsi), which led to an average 10±5 fold gain in focality in IL ($t(4)=2.84$, $p=0.047$, Fig 2E). However, further increases in the cancellation amplitude resulted in an increase in TI within MOp(ipsi) and a reduced focality, in line with the proposed cancellation mechanism. To validate the outlined cancellation principle, we calculated the distances between the minima of the cancellation curves that corresponded to cancellations in three brain regions: MOp(contra), Mop(ipsi), and IL (Fig 2F). Statistical analyses revealed that the distances between MOp(contra)-Mop(ipsi) and IL-Mop(ipsi) were significantly higher than zero, whereas the distance between IL-MOp(contra) did not differ from zero for both *in-vivo* and *ex-vivo* designs (Fig 2G). These results are consistent with the anatomical location of the analyzed regions relative to the cancellation field (i.e., the position of the frontal electrode), further supporting our modelling work.

Finally, we compared the distances between the minima of cancellation curves for *in-vivo* and *ex-vivo* designs (MOp(contra)-MOp(ipsi), IL-MOp(ipsi)) (Fig 2G). Our results showed that MOp(contra)-MOp(ipsi) distance was greater in *ex-vivo* compared to *in-vivo,* whereas no significant difference was observed for IL-MOp(ipsi) (Fig S5). We argue that this selective change might occur since in *ex-vivo* experiments, the destruction of ion gradients at axons reduces the efficiency of a signal transmission between directly connected brain areas as for MOp(contra) and MOp(ipsi), but not for IL and MOp(ipsi) that do not have direct connections (Oh et al., 2014; Wang et al., 2020). The diminished efficiency in the signal transmission will lead to an increase in the electrical impedance and, consequently, an increase in the distance between the minima of the cancellation curves. Therefore, we suggest that for an optimal cancellation design (e.g. a geometric location and cancellation amplitude) researches may, also, use the existing knowledge of the brain connectome

TI stimulation of IL combined with fMRI.

We next sought to explore whether neural stimulation via TI would produce discernible and consistent brain-wide responses, including any potential off-target effects, using functional magnetic resonance imaging (fMRI) based on BOLD signals. To achieve this, we adopted an approach akin to that of Missey and colleagues (Acerbo et al., 2022; Missey et al., 2021), involving the chronic implantation of electrodes in mice. However, our implant was designed to be compatible with MRI, enabling TI stimulation to be performed during fMRI recordings, thereby referred to as TI-fMRI (see Methods). We surgically implanted mice with three electrode pairs permitting TI stimulation and cancellation in the IL region (Fig 3A, Fig S14). During each surgical procedure, we simultaneously conducted LFP recordings in the IL region during TI stimulation, enabling the recording of a cancellation curve, as demonstrated in Figure 2B. Consequently, for each implanted animal, we ascertained the specific cancellation weight required to minimize TI-induced stimulation, corresponding to the minimum point on the cancellation curve. Subsequently, during a scanning session (Fig 3A), we conducted successive BOLD fMRI scans to assess the comprehensive brain-wide response to TI stimulation using both the previously discussed dipole (Fig 1C) and front tripole configurations (Fig 2A). We contend that, given the ongoing debate regarding the fundamental mechanisms of TI (Budde et al., 2023; Cassarà et al., 2022; Mirzakhalili et al., 2020), the establishment of an animal TI-fMRI paradigm is of critical importance for two main reasons: (i) it demonstrates the elicitation and the mapping of a physiological response in the brain via TI stimulation and (ii) it allows to further investigate the effects of our proposed tripole configuration incorporating a cancelling field.

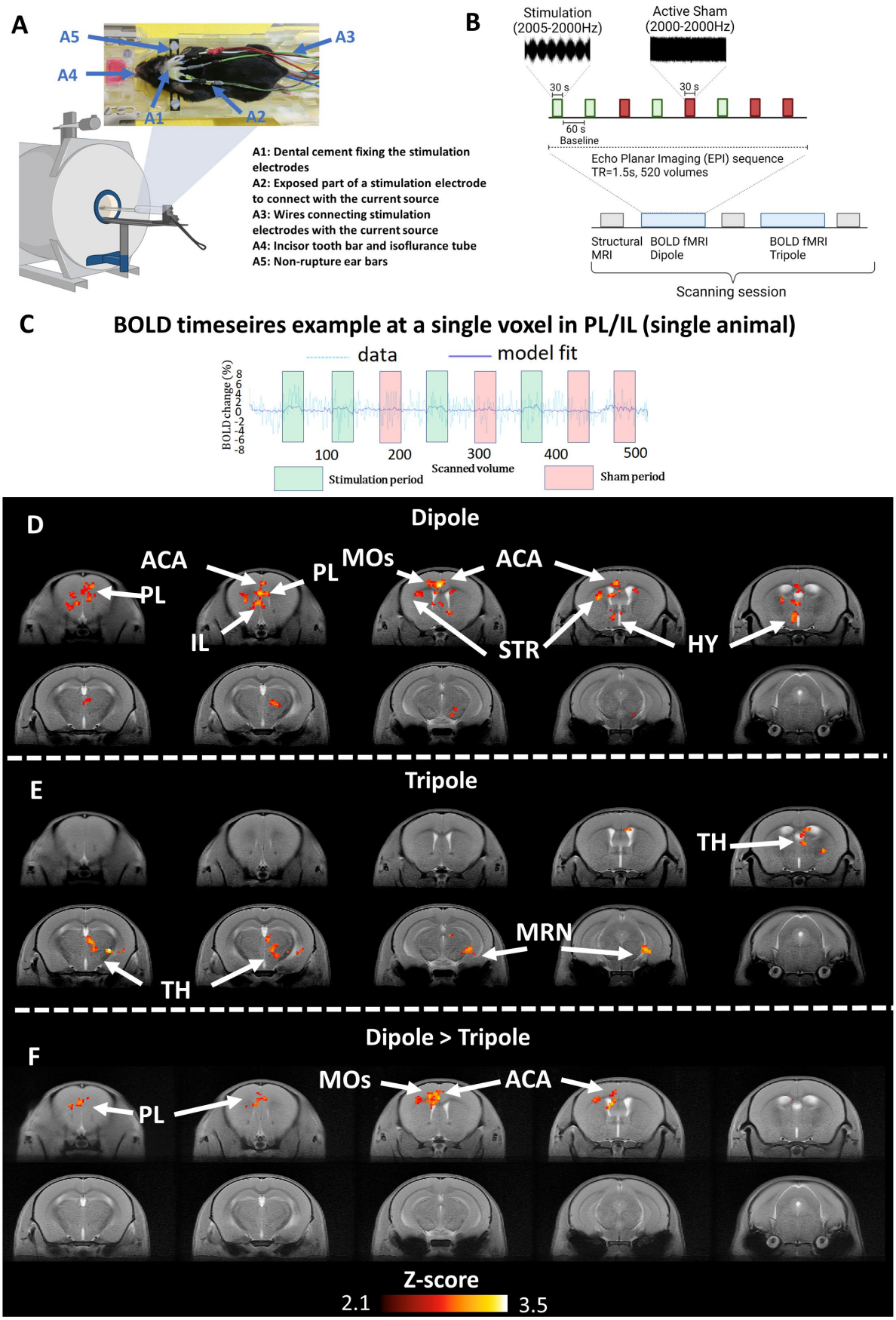
A
A5
A4
A3
A1
A2
A1: Dental cement fixing the stimulation electrodes
A2: Exposed part of a stimulation electrode to connect with the current source
A3: Wires connecting stimulation electrodes with the current source
A4: Incisor tooth bar and isoflurance tube
A5: Non-rupture ear bars
B
Stimulation (2005-2000Hz)
Active Sham (2000-2000Hz)
30 s
30 s
60 s
Baseline
Echo Planar Imaging (EPI) sequence
TR=1.5s, 520 volumes
Structural MRI
BOLD fMRI Dipole
BOLD fMRI Tripole
Scanning session
C
BOLD timeseires example at a single voxel in PL/IL (single animal)
data
model fit
BOLD change (%)
8
6
4
2
0
-2
-4
-6
-8
100
200
300
400
500
Scanned volume
Stimulation period
Sham period
D
Dipole
ACA
PL
PL
IL
MOs
ACA
STR
HY
E
Tripole
TH
MRN
TH
F
Dipole > Tripole
MOs
ACA
PL
Z-score
2.1
3.5

Figure 3. Whole-brain effects of TI stimulation exposed by fMRI.

A: TI-fMRI experimental setup and the main components of a chronic implant **B:** Scheme of the applied stimulation protocol. **C**: Representative example of the BOLD timeseries **D-F:** Coronal projections featuring the main hotspots induced by dipole and tripole TI stimulation, as well as the areas showing higher statistically significant activation in dipole compared to tripole. Heatmap represents general linear model results (e.g. z-scores) at the group level (n=5). TI-Active Sham contrast is shown. ACAv- Anterior Cingulate Area, ventral part, ACAd- Anterior Cingulate Area, dorsal part, MNR- Midbrain reticular nucleus, MOs- Secondary Motor Area, PL/IL- Prelimbic/Infralimbic area, STR- striatum, TH- Thalamus, HY- Hypothalamus.

First, we used the previously described dipole design (Fig 1C) to check whether the amplitude used for electrophysiological recordings (e.g. 5µA) is sufficient to elicit BOLD response. We conducted eight 30-second blocks of either TI or Active Sham stimulation, mixed in a pseudorandomized order, with 60-second pauses in between (Fig 2B). At the 5µA, we were unable to detect any discernible BOLD activation, which can be attributed to the relatively subtle impact of TI-elicited LFP and neural spiking activities within this low amplitude range. However, when we employed dipole TI stimulation with an amplitude of 700 µA, a current previously used to trigger a motor response (Acerbo et al., 2022; Missey et al., 2021; S. X. Song et al., 2021), we observed a robust activation not only within the targeted infralimbic area but also in adjacent regions such as the Anterior Cingulate Cortex (ACA), secondary motor cortex (MOs) as well as in the striatum (STR), midbrain reticular nucleus (MNR), thalamus and hypothalamus (Fig 3D). No activation was detected for Active Sham stimulation at the group level (see Discussion for more details). We argue that while ACA / MOs activation may result from off-target TI stimulation and/or cortico-cortical connections (Le Merre, Ahrlund-Richter, & Carlen, 2021), the activation of the striatal, midbrain, thalamic and hypothalamic areas without the recruitment of the neighbouring regions is most likely caused by the activation of a motor network (e.g. MOs, STR and MNR) as well as cortico-thalamic and cortico-hypothalamic networks (Le Merre et al., 2021; Schaeuble & Myers, 2022; Wang et al., 2020; Xue et al., 2022). In our second-level analysis, when comparing dipole stimulation with tripole stimulation, we observed a significant reduction in BOLD responses within the targeted cortical areas indicating an effective TI-field cancellation with front tripole configuration (Fig 3D). The comparison between tripole stimulation and the Active Sham condition revealed clusters of activation primarily localized within thalamic nuclei and midbrain, spanning both

the dorso-ventral and anterior-posterior axes. Notably, the synchronous absence of TI-induced activation in prefrontal structures such as the IL and MOs alongside with hypothalamic and striatal areas during TI tripole stimulation aligns with our hypothesis that the hypothalamic and striatal activations observed in the dipole design may be attributed to the activation of the cortico-hypothalamic and cortico-striatal networks (Schaeuble & Myers, 2022; Wang et al., 2020). In summary, our chronic and MRI-compatible brain implant permits TI stimulation on mice alongside BOLD fMRI (e.g. TI-fMRI) to study whole-brain network effects for dipole and tripole designs.

Discussion

Optimizing Temporal Interference Focality through Phase-Active Cancellation

Temporal Interference (TI) stimulation has grown in popularity in recent years as it allows for non-invasive stimulation of deep brain structures for both preclinical investigations (Acerbo et al., 2022; Botzanowski et al., 2023; Botzanowski et al., 2022; Missey et al., 2022; Missey et al., 2021; S. X. Song et al., 2021) and applications in human subjects (Acerbo et al., 2022; Collavini et al., 2021; Ma et al., 2022; Missey et al., 2023; Violante et al., 2022; Wessel et al., 2021). At the same time, recent work has unveiled instances of off-target stimulations during *in-vivo* TI on rodents and *ex-vivo* TI on human cadavers (Acerbo et al., 2022; Budde et al., 2023; Missey et al., 2021), a phenomenon previously foreseen through *in-silico* modeling (Mirzakhalili et al., 2020). Combined, these results provide compelling evidence that TI stimulation leads to a spatial sequence of tonic and phasic neural activations alongside a high-frequency conduction block (i.e. 'sandwich' hypothesis (Mirzakhalili et al., 2020)) underscoring prospective challenges in achieving precise focal targeting of a predefined brain area. This poses a significant issue as it hinders the ability to specifically target and manipulate distinct brain regions, potentially leading to unintended and confounding effects in neuroscience and clinical applications.

In the current investigation, we adopt a multi-level approach and propose a solution to increase focality for TI stimulation. This involved the development of a computational modeling approach to identify the most effective electrode placements for precise targeting of the prefrontal cortex in mice with two interfering electric fields – dipole TI stimulation. The induced effects of dipole TI stimulation were characterized through *in-vivo* and *ex-vivo* measurements with LFPs recordings and fMRI. These measurements enabled us to elucidate the presence of off-target TI effects in distant brain regions. Importantly, we observed that neither the optimal TI steering, nor the reduction of the stimulation amplitude eliminated these off-target effects, additionally highlighting the limitations of the commonly used (Acerbo et al., 2022; Botzanowski et al., 2022; Missey et al., 2021; Violante et al., 2022; Wessel et al., 2021) dipole design. We further proposed tripole configuration for TI stimulation to diminish off-target TI effects and to boost spatial focality. Tripole configuration complements previously discussed dipole design with an additional pair of electrodes producing an electrical field with an active (e.g. source-driven) phase shift in relation to dipole fields. Using tripole TI

stimulation with a 180-degrees shifted additional field (i.e. cancellation field), we achieved a selective decrease of TI fields in an off-target area, without affecting our main region of interest. Finally, we proposed a mechanistic explanation of how a tuned combination of constructive and destructive interferences result in the selective TI cancellation and verified the proposed mechanism with LFPs and fMRI. We argue for the prospective employment of active phase-driven TI cancellation in already existing multipair designs (Botzanowski et al., 2023; Budde et al., 2023; Cao & Grover, 2020; X. Song et al., 2021).

Further prospectives for TI-fMRI

The assessment of TI off-target effects with LFPs relies on a-priori hypothesis driven by existing neuroanatomy and our understanding of TI biophysics. However, the latter is currently a subject of ongoing debates and, as suggested by recent *in-silico* and *in-vivo* studies, TI can drive changes in activity in multiple spatially distant regions (Budde et al., 2023; Mirzakhalili et al., 2020) which, in their entirety, can hardly be captured with spatially restricted LFPs. Therefore, a comprehensive assessment of TI stimulation effects should include whole-brain imaging techniques such as fMRI (for other whole-brain imaging techniques see (Markicevic, Savvateev, Grimm, & Zerbi, 2021)). With this in mind, we believe that the developed an MR-compatible chronic implant enabling TI stimulation alongside fMRI scanning (i.e. TI-fMRI) opens new avenues for the preclinical research of TI stimulation. Specifically, using TI-fMRI, we were able to show the activation of the target cortical region and associated cortio-striatal, cortico-thalamic and cortico-hypothalamic networks. Additionally, we showed that phase-active cancellation concept can be successfully applied by using tripole TI configuration in an fMRI setting, allowing to assess the whole-brain effects of multipair TI stimulations.

An important direction that a chronic design of the MR-compatible implant unfolds is an opportunity to study TI-induced behavioral effects and whole-brain network perturbations on the same animal and, in case of awake rodent fMRI (Han et al., 2019), within the same experiment, mimicking the design of recent human-based TI-fMRI experiments (Violante et al., 2022; Wessel et al., 2021). This matching between animal and human-based experimental designs could allow the application of TI in parallel for bench experiments and patient trials, thus, significantly advancing both basic and clinical research.

Limitations

Limitations of the current practical setup

One of the goals of the current work was to provide the empirical demonstration of a strategy for increased focality for TI stimulation, supported by computational modelling. Hence, our primary emphasis revolved around the comprehensive assessment of TI fields, specifically through the analysis of local field potentials across a wide spectrum of brain regions. Simultaneously, we employed whole-brain fMRI to capture global responses. It's worth noting that, in contrast to other methodologies like calcium imaging and patch-clamp cell recordings, our approach did not involve the direct quantification of neuronal activity in our investigations. Instead, we relied on LFPs and fMRI to provide valuable insights into the broader neural responses elicited by TI stimulation. It is noteworthy to mention that a recent investigation conducted by Carmona-Barron and colleagues identified augmented signals in c-fos and GFAP staining within blood vessel cells of rat brains following TI stimulation. As a result, there remains uncertainty regarding the potential impact of TI on blood vessels and whether such direct effects might contribute to the observed BOLD fMRI responses. (Carmona-Barron et al., 2023). Despite these considerations, our study contributes to the ongoing efforts to refine TI stimulation techniques and gain a deeper understanding of its effects using tools applicable to humans and thus offering valuable insights into its potential applications in the clinic.

Direct effects of Active Sham stimulation

While effectively reducing TI fields in the desired region of interest, our TI-fMRI experiment also showed that Active Sham stimulation with tripole configuration leads to significant, brain-wide BOLD changes detected with both single-animal and group-level analysis (Fig S8 and S9). Analysis of the data from individual animals during dipole stimulation, also, exposed cortical and subcortical BOLD changes during Active Sham condition for all (n=5) analysed animals (example on Fig S6 and S7). Importantly, Active Sham-driven activations were present during Active Sham condition and absent in the pause periods (Fig S6-8B), allowing us to conclude that these activations were not post-effects of TI-stimulation and were directly triggered by Active Sham stimulation. We argue that Active Sham-driven BOLD changes were not found at the group analysis for dipole configuration because of the substantial spatial variability of Active Sham-induced hotspots across the animals at dipole TI-fMRI. At the same time, the use of an additional kHz field in the tripole configuration further amplified Active Sham-induced

effects permitting their detection at the group-level analysis. Therefore, while the usage of multipair designs permits the increase in the spatial focality of TI stimulation, it, also, amplifies effects of kHz stimulation, as high-frequency conduction block. It is, also, important to consider the effects of kHz stimulation when making causal inferences between detected changes in brain activity and applied TI stimulation. For instance, using fMRI we exposed an activation hotspot comprised from voxels activated by both TI and Active Sham stimulations (Fig S7-8). Such "dual nature" of TI-triggered brain activation additionally highlights a caution researchers should take when describing TI-induced effects. We suggest that by coupling fMRI recordings with the direct recordings of neural activity by, for instance, calcium imaging (Schlegel et al., 2018) , one can analyse the temporal frequency of neural firing and ultimately distinguish between activations induced by TI and effects of kHz fields.

Since the current study focused on (i) developing a method to refine TI-induced stimulation hotspot and (ii) to combine TI stimulation with fMRI, our focus was not directed towards a comprehensive exploration of the origins of Active Sham induced effects. Instead, our tripole TI-fMRI experiment was designed to substantiate the cancellation concept previously demonstrated with electrophysiological data.

Conclusion

In summary, our study not only empirically identified the presence of off-target TI fields but also introduced and provided a mechanistic understanding for a novel active phase cancellation approach permitting the boost of the spatial precision of TI stimulation. This innovation has the potential to be seamlessly integrated into current TI protocols for both rodent and human research. Furthermore, the combination of TI with fMRI represents a promising avenue for evaluating empirically the effects of TI stimulation throughout the entire brain, serving as a bridge between animal-based TI research and human studies.

Methods

Animals

All animal experiments were performed under license from the Zürich Cantonal veterinary office following Swiss federal guidelines for the use of animals in research. For the experiments C57BL/6J mice (Charles River Laboratories, Germany) were used. Animals were housed in a group of five with 12-hour light/dark cycle and *ad libitum* food.

In-vivo electrophysiology

Surgical procedures

The mice were initially anesthetized with 4% isoflurane (in a 1:4 O2: air mixture as the carrier gas). The anesthesia condition was verified by assessing pedal withdrawal reflex. The mouse head was placed in a stereotaxic head frame between non-rupture ear bars on a heating pad. The animals' body temperature (with the rectal probe) and respiration rate was monitored by the experimenter. Animals were kept in the anesthetized state with 1-2% isoflurane throughout the experiment. Prior to the start of the surgical procedure 0.1 ml of 1% lidocaine was injected subcutaneously into the scalp above the surgical region, 2-3 min later the area was shaved and disinfected with 70% Ethanol solution and the surgery started.

The scalp was opened, and the craniotomies were performed for a prospective electrode's implantation. All coordinates were calculated using Paxinos Atlas (Third Edition, 2007). *Dura* matter was removed, and stimulation electrodes (PVC insulated solid-core copper wire, 0.65 mm (22 AWG) diameter, PRT-11367 Distrelect) were placed on top of the brain tissue according to the craniotomies listed in Table S2 "Front Cancelling". Recording electrodes (34 AWG wires from 18-pin Wire Adapter, Part #B7600 Intan Technologies ©) were placed according to the stereotaxic coordinates listed in Table S2. Ground and reference electrodes were bound together and twisted before the implantation in the Cerebellum. Upon the completion of *in-vivo* recordings assigned to "Front Cancelling" design, recording electrode from HIP_{IPSI} was removed and the source electrode from the cancellation pair was put at HIP_{IPSI} AP/ML coordinates on the brain surface for "Lateral Cancelling" experiment (Table S2).

At the end of *in-vivo* experiments animals were sacrificed via cervical dislocation. After waiting for at least 1h, *ex-vivo* experiments were performed on the cadavers using the same electrode locations (Tables S2). For transcranial electrophysiological recordings electrodes from

stimulation and cancellation pairs were placed on the skull surface next to the corresponding craniotomies.

Electrical Stimulation

Three DS5 Isolated Bipolar Constant Current Stimulators (Digitimer©) were used as current sources and were driven by the input from data acquisition card NI cDAQ 9174 (National Instruments©) to produce the desired fields. For Dipole configuration one of DS5s was not used. Data acquisition card was connected to the PC allowing the manual adjustment of the field parameters via Matlab scripts.

Electrophysiological recordings

Local field potentials (i.e. LFPs) were recorded by recording electrodes using RHS Recording Controller (Part M4200, Intan Technologies ©) with RHX Data Acquisition Software at 20 KHz sampling rate. The following post-processing steps were applied to the recorded time series using a custom-built Matlab script to extract TI-induced oscillations (Fig S10).

The principal post-processing steps included: (i) uploading the data using read_intan_RHS2000_file provided by Intan Technologies© (ii) detecting the envelope with the custom Matlab© script using a modified version of Hilbert transformation ameliorating Gibb's distortions (Schreglmann et al., 2021) along with bandpass (from 0.1Hz till 250Hz) causal filtering similarly as was done in (Missey et al., 2021),

(iii) smoothing of the detected envelope by using a sliding window of 2 sampling units,

(iv) convolving the envelope with a complex Morlet wavelet at TI frequency to extract the oscillation at TI frequency(Cohen, 2019),

$$f(t) = (e * m')(t) = \int_0^t e(\tau)m'(t-\tau)d\tau \ (1)$$

Where e is the extracted envelope signal, m' is the Morlet wavelet and t is the analyzed recording time.

(v) f(t) analytic signal is used to extract the signal phase and amplitudes according to equations 2-3,

$$Phase = Im\big(f(t)\big) \ (2), Im - imaginary\ part$$

and

$$Amplitude = DFT\left(Re\left(f(t)\right)\right) (3), DFT - Discrete\ Fourier\ Transform;\ Re - \ real\ part$$

Phase-lag index is additionally computed to verify the presence of a phase shift between oscillations from different regions(Stam, Nolte, & Daffertshofer, 2007). To ensure that the observed oscillation at TI frequency (e.g. 5 Hz) is not caused by the passive intermodulation(Lui, 1990) between the high-frequency oscillations (e.g. 2000 and 2005 Hz) we verified the absence of an increased harmonic at TI frequency in Fourier Spectrum of the raw signal (e.g. before extracting the envelope as described in step (ii)).

For the processing of tACS data, the same pipeline but without envelope extraction (step (ii)) and intermodulation detection was used.

Temporal Interference combined with fMRI.

Chronic implant design

Electrodes were made from Teflon-Coated Silver Wires 0.25 mm (AFT1010, World Precision Instruments, Germany). One side of the wire was placed on top of the cortex, whereas the other side was used to connect to the current sources via a single minipin (DIL-Socket Flachprofil, 85366930, RS Components, Frankfurt am Main, Germany) soldered to the tip of the wire. To increase the stability of the chronic implant, an additional co-axial isolation was implemented using co-axial heat shrinkage PTFE tubes (0.38 mm TFE2-30-1220, 0.46 mm TFE2-28-1220, 0,56mm TFE2-26-1220 from Distrelec, Switzerland). To avoid the lateral contact between mini-pins, each of the min-pin was isolated using 2.5 mm heat shrinkage tube (RND 465-00234, Distrelec, Switzerland). An optimal length of the wire is between 2.0 and 2.5 cm, the longer wires were more fragile and were removed by the animals during the post-surgery recovery, whereas too short wires resulted in the close position of the mini-pin to MRI cryo-coil causing distortions of the scanner magnetic field. The Teflon isolation was then removed from the wire and its tip placed on the cortex. We recommend removing the isolation not only from the wire tip, but also an additional 0.5 mm starting from the tip. This ensures a stable contact between the wire and the brain. Fig S14 A depicts an example of the used electrode with all described elements.

Stereotaxic surgery

The mouse was initially anesthetized with 4% isoflurane (in a 1:4 O2: air mixture as the carrier gas). Intramuscular injection of a mixture of fentanyl (0.05 mg/kg), midazolam (5 mg/kg) and

medetomidine (0.5 mg/kg) was performed ensuring the stable anesthesia for the whole duration of stereotaxic surgery. The following surgical procedures and craniotomies were performed as described in "*In-vivo* electrophysiology section" using coordinates from Table S2 "Front cancelling", but with 0.25 mm Teflon-isolated silver wires (AFT1010, World Precision Instruments, Germany) used as stimulation electrodes. Custom-made chronic implants were fixated to the skull with dental cement (Optibond Solo Plus, M+W Dental Swiss AG, Switzerland). Recording electrodes were connected to electrodes (34 AWG wires from 18-pin Wire Adapter, Part #B7600 Intan Technologies ©) from RHS Recording Controller (Part M4200, Intan Technologies ©). The Teflon-isolated silver wire and the mini pin were used as recording electrodes for IL and Ground respectively (Table S2). Ground and reference electrodes from RHS Recording Controller were bound together and twisted before the connection to the minipin placed in the Cerebellum (Table S2).

LFPs recordings were performed and processed as previously discussed in "*In-vivo* electrophysiology section" section (Fig S10). We showed that the resulting TI cancellation curve was well fitted with a double Gaussian both for individual animals and at the group level, hence reproducing the results discussed for acute electrophysiology (Fig S13). Upon the completion of the TI cancellation experiment, the recording electrodes were removed and the remaining exposed skull surface covered with dental cement (Fig S14). Cancellation field amplitude causing the minimum TI field in IL was used in the follow-up TI-fMRI experiment, therefore, allowing a subject-tuned cancellation.

500 µl of Saline solution was s.c. injected to ameliorate a potential dehydration. Upon the finish of the surgery antagonist-antidote mixture was injected into the mouse consisting of temgesic (0.2 mg/kg) and annexate (0.5 mg/kg). After the surgery animals were left in a wake-up cage that has a heating pad under it until they wake up and show locomotor activity. Animals were then returned to their home cages and were single housed for the whole post-recovery phase. During the first 3 days after the surgery analgesic (Ketoprofen (10 mg/kg)) was administered daily to ameliorate a potential pain during the postsurgical recovery. At the post-surgery recovery phase all animals showed no pain symptoms, and the implant did not hamper the animal's locomotor activity.

TI-fMRI experiment

MRI acquisition parameters

MRI sessions were performed using 7-T Bruker BioSpec scanner equipped with a PharmaScan magnet with transmitter-receiver cryogenic coil (Bruker BioSpin AG, Fällanden, Switzerland). Adjustment procedures included wobbling, reference power and shim gradients adjustments using Paravision v6.0. Echo Planar Imaging (EPI) sequence was used for BOLD fMRI acquisition with the following parameters: repetition time (TR) = 1.5 s, echo time (TE) = 15 ms, flip angle = 60°, matrix size = 90 × 50, in-plane resolution = 0.2 × 0.2 mm2, number of slices = 20, slice thickness = 0.4 mm, and 520 volumes. Each MRI scan was accompanied by 8 Temporal Interference blocks. Each block has the following structure with either Stimulation or Active Sham condition: 60s baseline, 1s ramp-up, 30s Stimulation or Active Sham, 1s ramp-down, 1s post-baseline.

The MRI preprocessing steps, and General Linear Model (GLM) analysis were conducted using FSL FEAT (version 6) and custom-build Matlab scripts. In short, preprocessing steps included high-pass filtering (cutoff of 100s), motion correction using MCFLIRT and spatial smoothing using a Gaussian kernel with FWHM 0.5mm. The data were registered to study-specific standard space template using linear normal search and 12 degrees of freedom (DOF) options. Temporal filtering was applied on each voxel timeseries to remove the autocorrelation with FILM (FMRIB's Improved Linear Model) (I.e. FILM prewhitening). Finally, the extracted timeseries were processed with voxel based GLM – first level analysis. The experimental design (e.g a temporal sequence of Stimulation and Active Sham conditions) convolved with double-gamma hemodynamic response function and its derivative, as well as standard motion parameters (MCFLIRT) were used as explanatory variables (EVs). All EVs underwent the same high pass filtering as was previously applied for the raw data. Z-statistics were computed with cluster thresholding $p<0.05$ and $z>1.9$. For the second-level analysis, to compare whole-brain maps between two conditions (e.g. dipole and tripole) we used fixed effects (FE) modelling feeding the results of the corresponding first-level analysis as inputs.

Hardware for Temporal Interference stimulation

Three DS5 Isolated Bipolar Constant Current Stimulators (Digitimer ©) were used as current sources and were driven by the input from data acquisition card NI cDAQ 9174 (National Instruments ©) to produce the desired fields. Stimulation electrodes from the implant were connected to the DS5 stimulators with MRI-compatible cables and electrodes (neuroCare

Group GmbH, Germany) via Radio Frequency (RF) filter module (neuroCare Group GmbH, Germany). To ensure that no damage was introduced to the implant wires during the post-surgery recovery time, the impedance between stimulation pairs was measured prior to the experiment using NeuroConn DC-Stimulator (neuroCare Group GmbH, Germany). In addition, to ensure that the wires from the current stimulator and the implant were not disconnected from each other due to an accidental movement of the animal during the scan, the impedance measurements were repeated prior to every stimulation session.

Anesthesia for fMRI experiment

All mice were initially anesthetized with isoflurane (in a 1:4 O2: air mixture as the carrier gas): 4% for induction and endotracheal intubation. Endotracheal intubation was performed as previously described in (Grimm, Wenderoth, & Zerbi, 2022). After the animal was placed in the MRI bed, it was connected to a small animal ventilator and mechanically ventilated at a rate of 90 breaths/min, with isoflurane set to 1%, with a respiration cycle of 25% inhalation, 75% exhalation, and an inspiration volume of 1.8 ml/min.

The mouse head was immobilized using an incisor tooth bar and non-rupture ear bars. Body temperature was measured using a rectal temperature probe and maintained at 36.5± 0.5°C by means of a warm-water circuit integrated into the animal holder (Bruker Biospin GmbH, Ettlingen, Germany). Following the animal preparation, the tail vein was cannulated for intravenous (i.v.) administration of a bolus of 0.05 mg/kg medetomidine (Domitor, medetomidine hydrochloride; Pfizer Pharmaceuticals, Sandwich, UK). After 10 minutes continuous infusion of medetomidine (0.1 mg/kg/h) is started. Isoflurane was lowered to 0.5%. After 20 minutes from the start of continuous medetomidine infusion MRI sessions were launched. An anesthesia solution was freshly prepared every day, by mixing saline and stock solution of medetomidine 1 mg/ml. Bolus volume and infusion rate were adjusted to the animal body weight to match the desired dose.

Computational modelling

Dipole modelling

***Model construction*:** While the level of segmentation improves the predictive power of the simulations, a mouse model with the highest number of segmented tissues was chosen among the models available in the Sim4Life database to find an optimal configuration of electrodes for IL stimulation. The model was generated with whole-body MR images of a 3-week male

mouse (B6C3F1) and segmented into 50 elements, which included skin, fat, eye, cerebrospinal fluid, skull, muscles, tongue, and various brain structures. For the simulations, these structures were grouped into 31 tissues that had different conductivity values taken from low-frequency conductivity table of the IT'IS tissue properties database version 4.0.

The electrodes were placed on the model in accordance with the high-density EEG system used in mice, which consisted of 38 electrodes and covered the entire surface of the brain(M. Lee et al., 2011). As depicted in Fig 1A, the electrodes were represented in the simulation as cylinders with a diameter of 0.25 mm. However, it is worth noting that in the modeling pipeline, the electrodes were placed on the mouse's scalp rather than on the *dura* matter, which is the location of the electrodes in practical experiments.

The location of the IL area in the mouse brain model was determined by co-registering the corresponding mask with Allen Brain Common Coordinate Framework (ccv3) (Wang et al., 2020) which includes 213 segmented brain regions, among which bilateral infralimbic and prelimbic areas were identified as regions of interest (ROIs). Co-registration was performed in FSL 5.0 Flirt, followed by atlas alignment with the model in Sim4Life. Subsequently, surface mesh was generated from the ROIs using built-in functions in Sim4Life. The resulting highly segmented mouse model can be employed to assess the effectiveness of TI field for IL stimulation with different electrode configurations.

<u>*Quantification of TI exposure:*</u> During TI stimulation two distinct high-frequency waveforms, f1 (e.g., 2 kHz) and f2 (e.g., 2.005 kHz), are applied over the scalp, which differ in low frequency values – 5Hz. This results in a corresponding low-frequency amplitude modulation – hereafter referred as the TI field or exposure, which is calculated according to equation 4:

$$|TI(w_1, w_2)| = \begin{cases} 2\left|\overrightarrow{E_{w2}}(\vec{r})\right| \\ \dfrac{2\left|\overrightarrow{E_{w2}}(\vec{r}) \times (\overrightarrow{E_{w1}}(\vec{r}) - \overrightarrow{E_{w2}}(\vec{r})\right|}{\left|\overrightarrow{E_{w1}}(\vec{r}) - \overrightarrow{E_{w2}}(\vec{r})\right|} \end{cases} if \left|\overrightarrow{E_{w2}}(\vec{r})\right| < \left|\overrightarrow{E_{w1}}(\vec{r})\right| \cos(\alpha) \quad otherwise \quad (4)$$

where $\overrightarrow{E_{w1}}(\vec{r}) = w_1\overrightarrow{E_1}(\vec{r})$, and $\overrightarrow{E_{w2}}(\vec{r}) = w_2\overrightarrow{E_2}(\vec{r})$. $\overrightarrow{E_1}(\vec{r})$ and $\overrightarrow{E_2}(\vec{r})$ are the current normalized E-fields from both electrode pairs, while w1 and w2 are the input currents.

Identification of the most focal and efficient electrode configuration requires the calculation of E-field exposure for all electrode pairs. Instead of performing corresponding simulations for

all possible pairs ($N_{combinations}$ = 703) to save computational time, an approach based on the superposition principle was adopted that suffices with $N_{electrodes}$-1 = 37 simulations, from which all possible exposures can be computed by linear combination. This superposition approach encapsulates the idea that one electric field generated with two electrodes can be calculated as a normalized sum of $N_{electrodes}$-1 electric fields, where all electrodes are set as returning except for one.

Simulations of the electric fields (E-fields) were performed using 'Electro Ohmic Quasi-Static' finite element method (FEM) solver, which discretizes the model using adaptive, rectilinear grid. In order to apply the superposition principle, 37 simulations were prepared, with the Dirichlet boundary conditions being set to the electrodes. Specifically, all electrodes were assigned a stimulation of 0 V, except for one active electrode assigned a stimulation of 1 V in each simulation. The resolution of the grid was defined after a convergence analysis, that established the necessity of 0.05 mm resolution for each voxel to receive an accurate E-field calculation in the gray matter of the mouse model. Additionally, we compared the predictions of the gray matter activation in two simulations, which had different grid sizes: one of which was extended and included the head and torso of the model, while another, i.e., reduced grid, consisted only of the head of the mouse. While the predicted activations did not differ between extended and reduced models, to save the computational efforts we proceeded with generating simulations that had a reduced grid with 0.05 mm resolution, which resulted in 87 796 176 rectangular voxels per simulation. After the simulation was computed, the electric fields were down sampled to the grid with 0.1 mm resolution for each voxel to accelerate the calculation of the TI fields.

Tripole modelling

To model the cancellation effect of the antiphase field COMSOL 5.3 software was used. The software uses a finite element method (FEM) to solve Maxwell equations for the computation of the electrical field in the medium.

A 3D model of a mouse brain was extracted from Allen Brain Common Coordinate Framework (ccv3). This model was used in COMSOL to simulate the mouse brain. The following parameters were used for FEM meshing: maximum element size (1.06e-4), minimum element size (7.68e-6), maximum element growth rate (1.4), curvature factor (0.4), resolution of narrow regions (0.7)

The material was chosen as water with dielectric properties adjusted to brain grey matter values at TI carrier frequency (2000 Hz): electric conductivity (1.03e-1 S/m) and relative permittivity (9.4e+4)(Hasgall et al., 2022). Stimulation electrodes were embedded as copper (COMSOL built-in properties) and placed according to the coordinates listed in the stereotaxic procedure section.

5 µA current was applied to each of the electrode pairs with a stepwise increase of the cancellation weight to produce *in-silico* results listed in Fig S2. FEM meshing as well as the scheme of the simulated field lines are shown at Fig S11.

Statistical analysis

All statistical calculations were done with custom-made Python 3.7 scripts using SciPy, NumPy, and statsmodels toolboxes. Figures were generated with custom-made Python 3.7 scripts and with BioRender.com. The exact procedures used for each analysis step are listed below.

Data Normalization (for cancellation experiments only)

Computed amplitudes of electrophysiological recordings (see Electrophysiological recordings) from the cancellation experiments were normalized to minimize between the subject variability in absolute LFP values (see equations 5-8 and Fig S12):

$$NCW_{LEFT} = \frac{CW - CW(A_{min})}{CW(A_{min}) - CW(A_0)} \quad (5)$$

$$NCW_{RIGHT} = \frac{CW - CW(A_{min})}{CW(A_{plateau}) - CW(A_{min})} \quad (6)$$

$$NA_{LEFT} = \frac{A - A_{min}}{A_0 - A_{min}} \quad (7)$$

$$NA_{RIGHT} = \frac{A - A_{min}}{A_{plateau} - A_{min}} \quad (8)$$

where Canceling Weight (fraction of stimulation amplitude) – CW, LFP Amplitude – A: Normalized Canceling Weight – NCW, Normalized Stimulation Amplitude – NA

The suggested normalization brings individual U-shape curves to the common scale. Normalized Canceling weights (NCWs) vary from -1 to 1 with the minimum at 0, whereas Normalized Amplitudes (NAs) are at the range from 0 to 1. At the same time, the proposed normalization preserves the relative steepness of the cancellation curve arms (see individual data points in Fig S2 and Fig S4) which is directly linked to the studied cancellation effect.

Group comparisons

Data distributions were tested for normality by Shapiro-Wilk test(Shapiro & Wilk, 1965) and homoscedasticity (variance homogeneity) via Levene's test (Brown & Forsythe, 1974).

For n ≥3 groups, If homoscedasticity and normality of the distributions were confirmed, one-way ANOVA for independent groups or repeated measures ANOVA for paired groups were used, with unpaired or paired t-tests (Student, 1908) for post-hoc comparisons. In case of the violation of homoscedasticity Welch corrected version of ANOVA was used(Welch, 1951). If the data were not normally distributed Kruskal-Wallis rank-sum test for unpaired (Kruskal & Wallis, 1952) or Friedman ANOVA for paired groups (Friedman, 1939) were used, with Mann-Whitney U-test (Mann & Whitney, 1947) or Quade test (Quade, 1979) for post hoc comparisons.

For 2 groups, If homoscedasticity and normality of the distributions were confirmed paired or unpaired Student t-tests (Student, 1908) were used. In case of the violation of homoscedasticity, Welch version of t-test (Welch, 1947) was used. If the normality condition was not met, Mann-Whitney U-test(Mann & Whitney, 1947) or Wilcoxon Signed Rank tests (Wilcoxon, 1945) were used for comparisons between paired and unpaired groups respectively.

False Discovery Rate was controlled by using adaptive two-stage Benjamini-Krieger-Yekutieli technique (Benjamini, Krieger, & Yekutieli, 2006) to correct p-values for multiple comparisons.

Bootstrap

Normalized LFP data (see data normalization) from cancellation experiments were fitted with the sum of two Gaussian functions (equation 9) at individual and group levels (e.g., pooled data).

$$NA = A * \exp(-B(NCW - S)^2) + A_1 * \exp(-B_1(NCW - S_1)^2) + C \quad (9)$$

where NCW and NCA are normalized canceling weights and ampltidues
and $\mathrm{A, B, S, A_1, B_1, S_1}$ and C are function − free parameters

Bootstrap (N=300 iterations) confidence interval (25 to 75 percentiles) was computed to estimate the confidence of the obtained fit at the group level.

In short, for each iteration the data were resampled with the replacement keeping the size of the original sample (e.g. pooled data). Resampled data was fitted providing the values for the corresponding free parameters. The computed free parameters were used to generate the fitting curve (equation 9) with NCW step of 0.01. The NA values for the fitting curve were saved and the new iteration was launched.

Shifts between curves minima.

Formula (6) is used to calculate the shifts between curves' minima.

$$Shift(curve\ 1, curve\ 2) = \frac{CW(A1_{min}) - CW(A2_{min})}{\frac{CW(A1_{plateau}) + CW(A2_{plateau})}{2}} \quad (10)$$

where $CW(A1_{min})$ and $CW(A2_{min})$ correspond to the cancelling weights at the minimum amplitudes for the curves 1 and 2 respectively and $CW(A1_{plateau})$ and $CW(A2_{plateau})$ are cancelling weights at a plateau phase (see Fig S12 for the abbreviations corresponding to an individual curve).

Denominator at formula 10 normalizes the computed shift to the mean width of the analyzed curves.

Supporting information

Electrophysiology

Animals/Regions	MOp_{ipsi}	MOp_{contra}	HIP_{ipsi}	HIP_{contra}
1	15	5		
2	165	350	345	
3	0	345	160	
4	5	195	205	190
5		210		175
6	355	190	170	170
7		340		
8		235		105

Table S1. TI mean phase shifts relative to IL. Each cell contains a phase shift of the TI in the corresponding region compared to IL. Empty cells correspond to the cases when the amplitude of TI was not distinguished from the background signal.

Electrode type	Electrode location		AP	ML	DV
Recording electrodes	IL		+1.54	-0.3	-2.8
	MOp_{IPSI}		-0.5	-1	-1
	MOp_{CONTRA}		-0.5	+1	-1
	HIP_{IPSI}		-3.1	-2.8	-2.5
	HIP_{CONTRA}*		-3.1	+2.8	-2.5
	Ground (Cerebellum)		-6	-1	-2.5
Stimulating electrodes	Ipsilateral Stimulation pair	Source	+2.4	-2.15	surface
		Ground	+2.4	-1.46	surface
	Contralateral Stimulation pair	Source	+2.4	+2.15	surface
		Ground	+2.4	+1.46	surface
	Cancellation Pair (front)	Source	-0.5	+1.75	surface
		Ground	-0.5	-1.75	surface
	Cancellation Pair (lateral)	Source	-3.1	-2.8	surface
		Ground	-0.5	-1.75	surface

Table S2. TI-Ephys coordinates

Stereotaxic coordinates used for the electrophysiological recordings upon TI stimulation in "Front Cancelling" and "Lateral Cancelling" designs. * LFP in HIP_{CONTRA} was not measured at "Lateral Cancelling design".

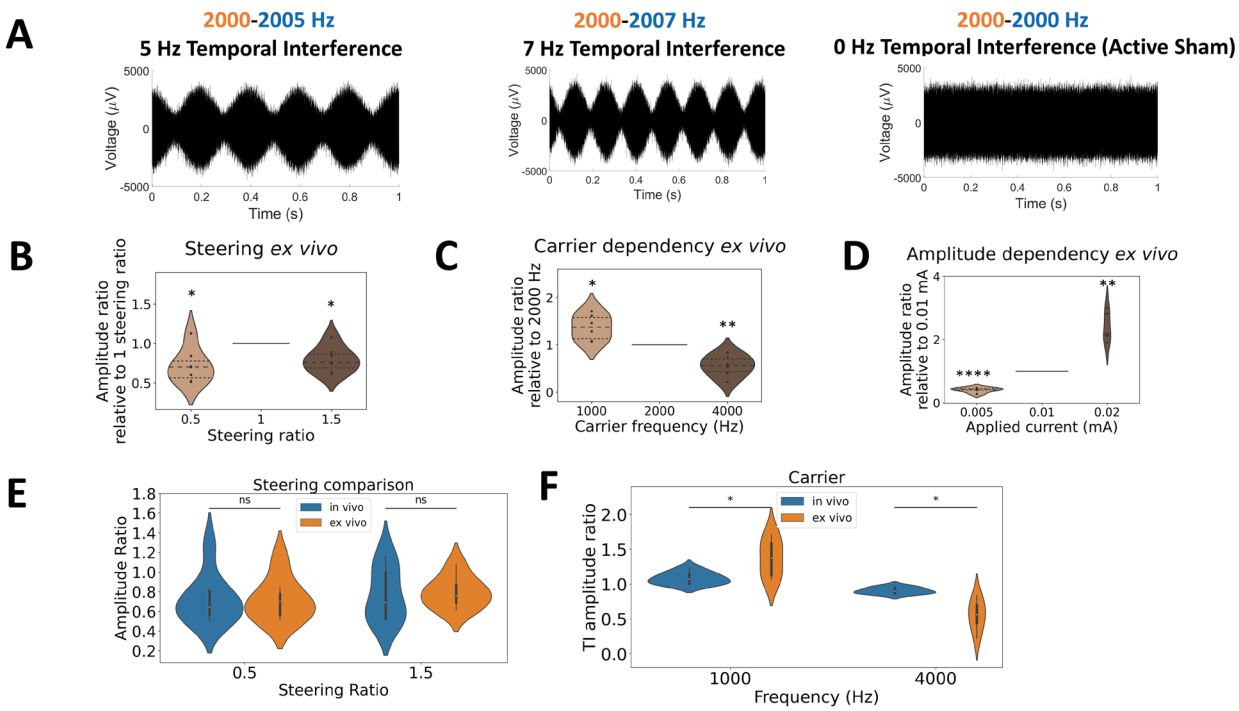

Figure S1. *Ex-vivo* electrophysiological assessment of dipole configuration.

A: Raw data examples of the envelope modulation (5 and 7 Hz) and Active Sham (0Hz) recorded in IL. **B.** Steering of TI amplitude outside of IL **C:** Dependence of TI amplitude in IL from the carrier frequency **D:** Scaling of TI amplitude in IL by changing currents applied to the stimulators **E:** Comparing TI amplitudes at both steering ratios between *in-vivo* and *ex-vivo.* **F.** Comparing TI amplitudes at different carrier frequencies between *in-vivo* and *ex-vivo.* ns- nonsignificant. *p<0.05, **p<0.01, ***p<0.001, ****p<0.001

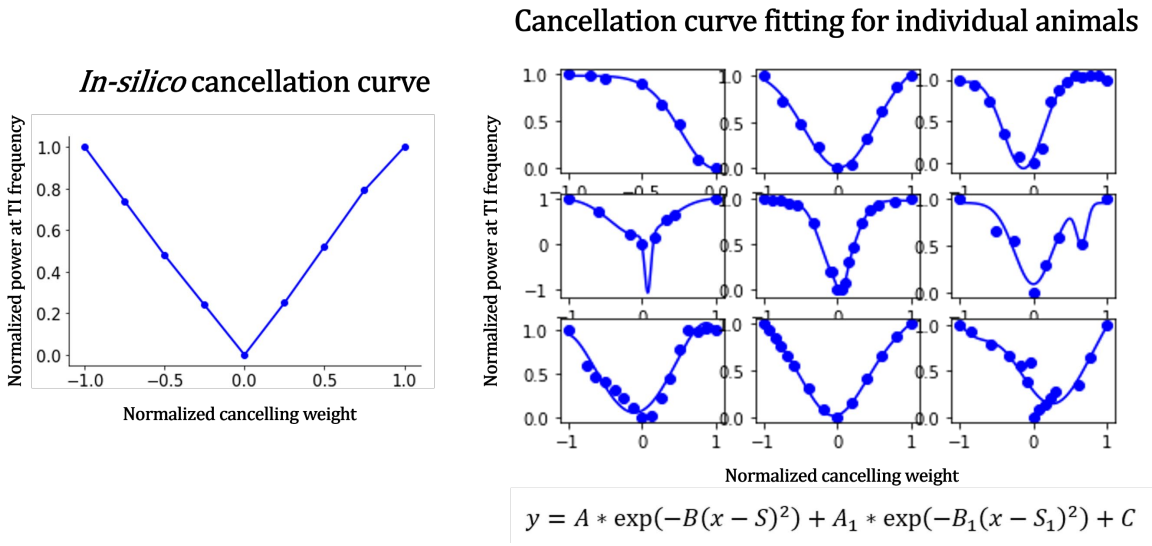

Figure S2. *In-silico* and individual *In-vivo* cancellation curves.

Modeled cancellation curve (left) and fitted cancellation curves for individual animals in-vivo (n=9) (right). Each chart represents the changes in Normalized TI amplitude alongside the increase of Normalized canceling weight. Dots represent individual data, whereas lines at the *in-vivo* plots (right) feature the fitting with the Double Gaussian curve (equation at the bottom).

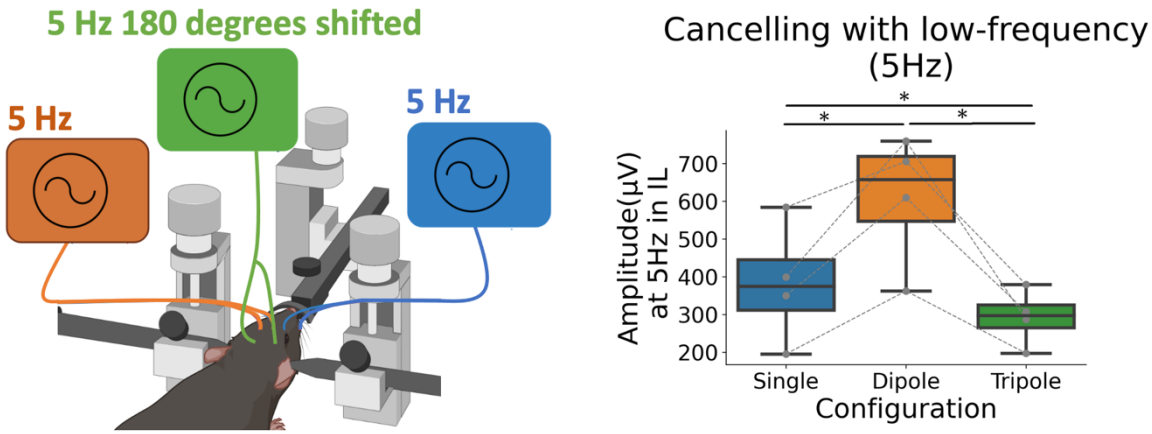

Figure S3. Low-Frequency cancelling field.

Cancellation effect at low frequency cancelling setup. Single (Ipsilateral electrode pair), Dipole (Ipsilateral and Contralateral) or Tripole (all pairs) were used to provide 5 Hz alternating current stimulation with the same amplitude (10 µA), but with 180-degree phase shift in cancellation pair. All conditions were tested at the same animals (n=4). ANOVA followed by paired t-tests was used to check for statistical significance. p-values are corrected for FDR. *p<0.05.

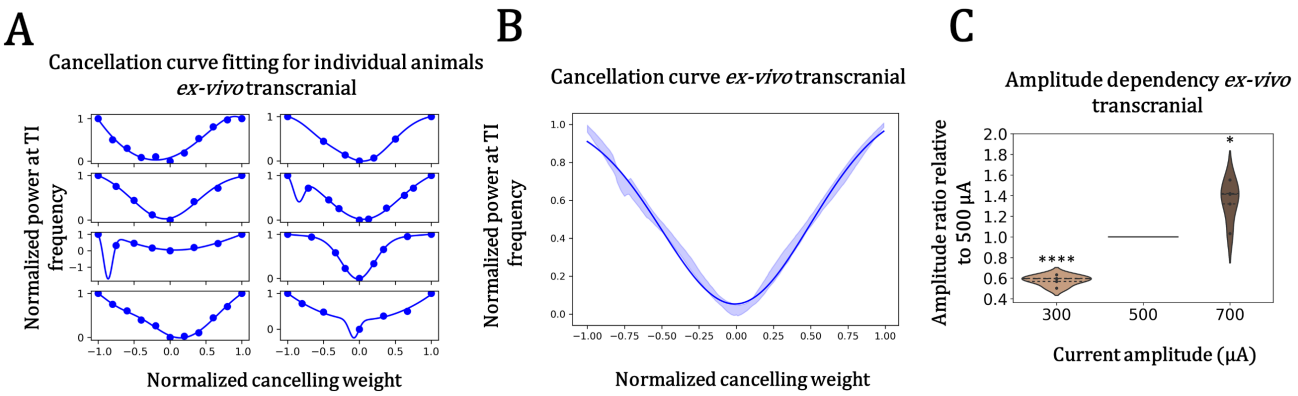

Figure S4. Ex-vivo transcranial TI cancellation.

A: Fitted cancellation curves for individual animals (n=8) **B:** TI amplitude in IL at different cancelling weights. Solid line represents the fitted model at the group level and shaded area depicts bootstrapped confidence interval (Q1 and Q3 percentiles) **C:** Scaling of TI amplitude by changing currents applied to the stimulators. *p<0.05, **p<0.01, ***p<0.001.

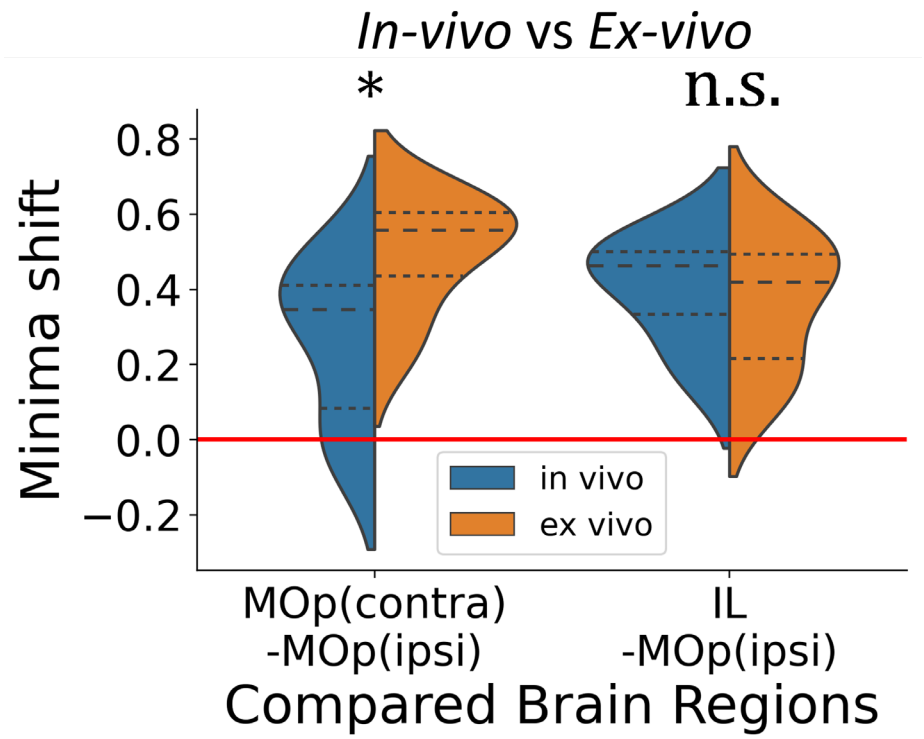

Figure S5. In-vivo vs Ex-vivo comparison of minima shifts.

Plot outlines the comparison between minima shifts for *in-vivo* and *ex-vivo* design (n=5). One-sided t-tests were used to check for the statistical significance. ns- not significant, *p<0.05

TI-fMRI

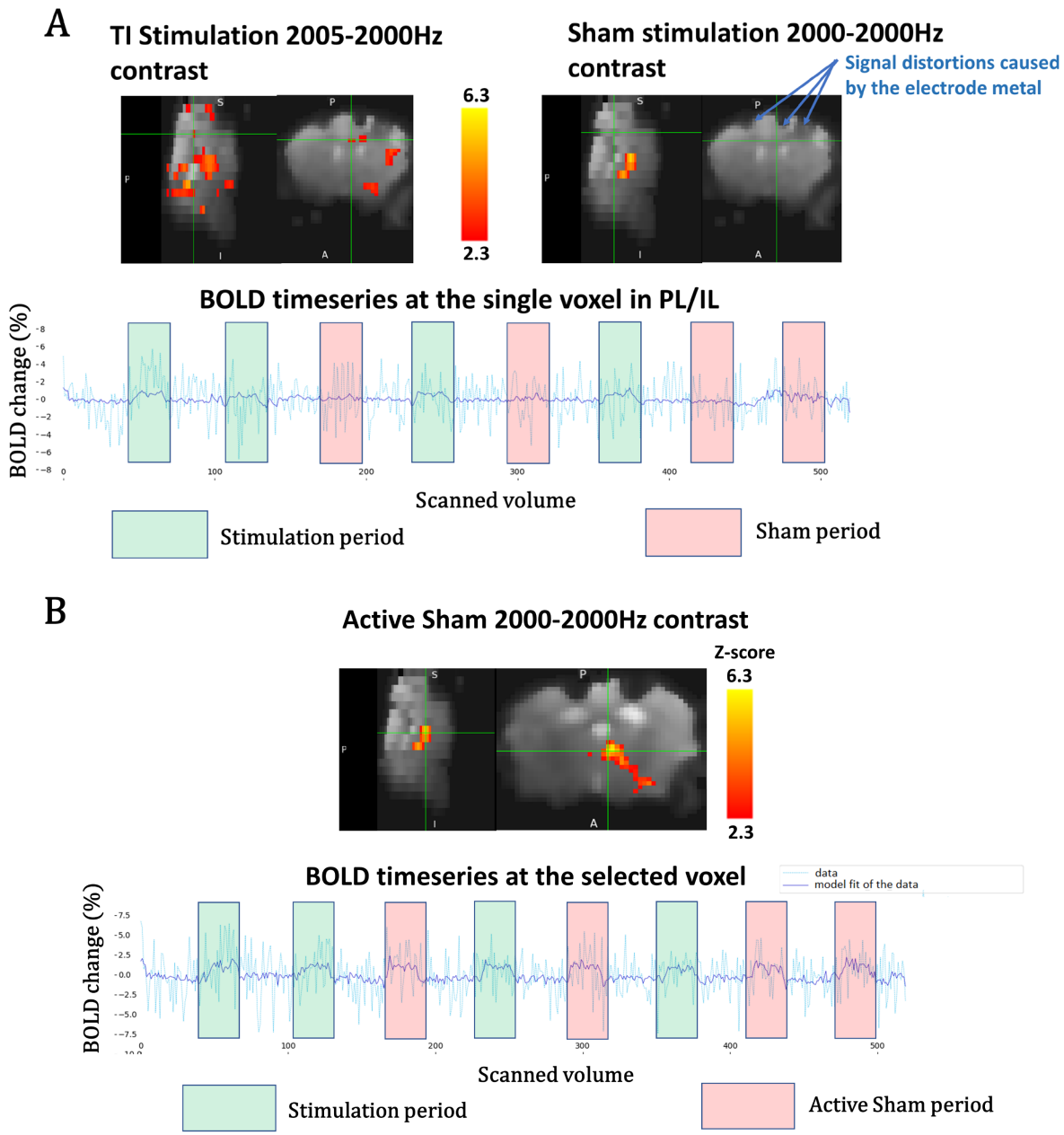

Figure S6. TI Stimulation and Active Sham for Dipole TI-fMIR. Single animal

A: TI stimulation and Active Sham contrasts along with BOLD timeseries at the selected voxel in Anterior Cingulate Cortex for a single fMRI session during TI dipole stimulation. **B:** Active Sham contrast and BOLD timeseries at the selected voxel in Thalamic area. For both TI and Active Sham conditions stimulation amplitude was 700 µA. Heatmap represents the results of general linear model analysis as z-scores.

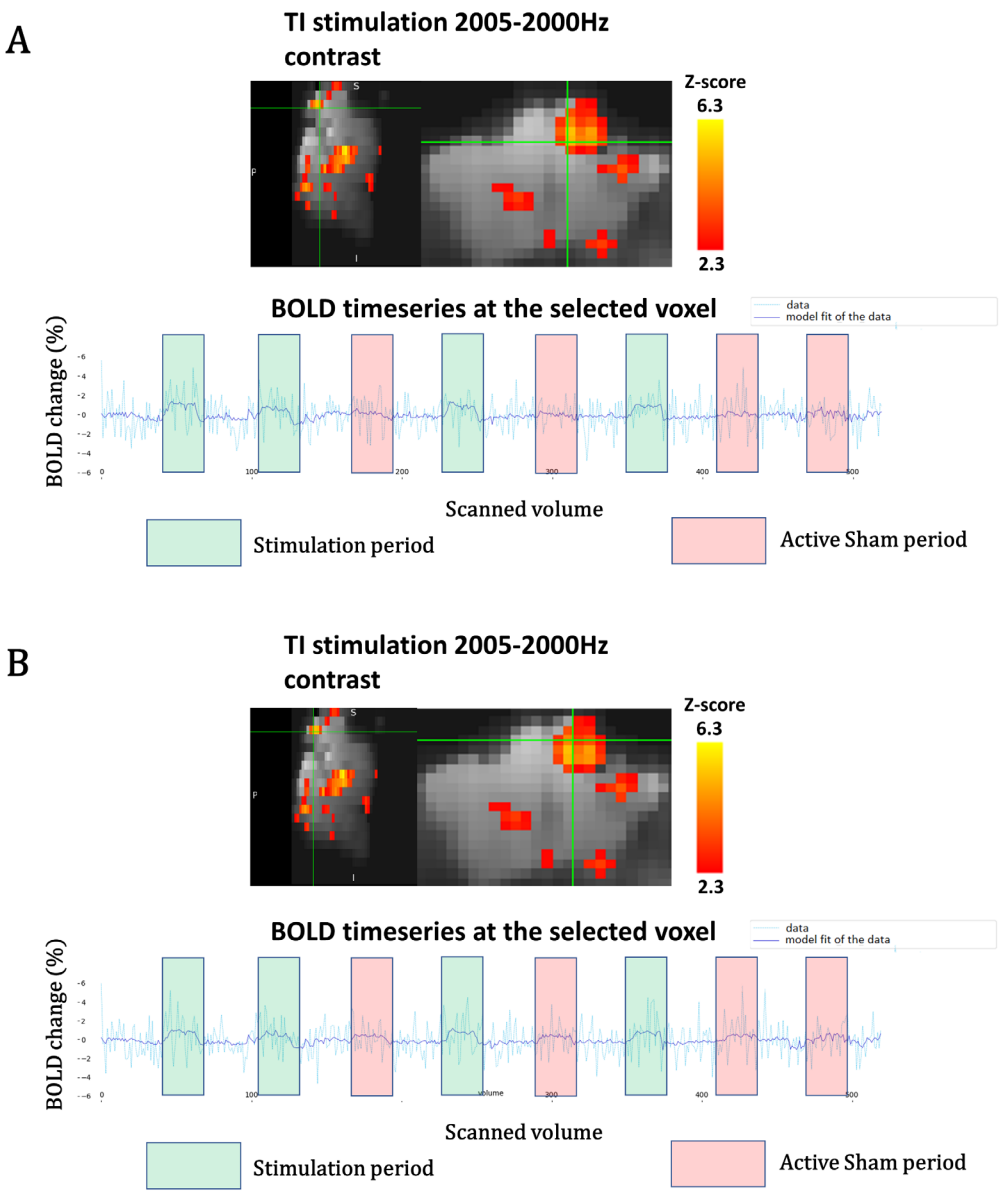

Figure S7. Dual nature of the off-target activation for Dipole TI-fMIR. Single animal

TI stimulation contrasts and BOLD timeseries at two different off-target voxels for a single fMRI session during TI dipole stimulation. Stimulation amplitude was 700 µA. Heatmap represents the results of general linear model analysis as z-scores.

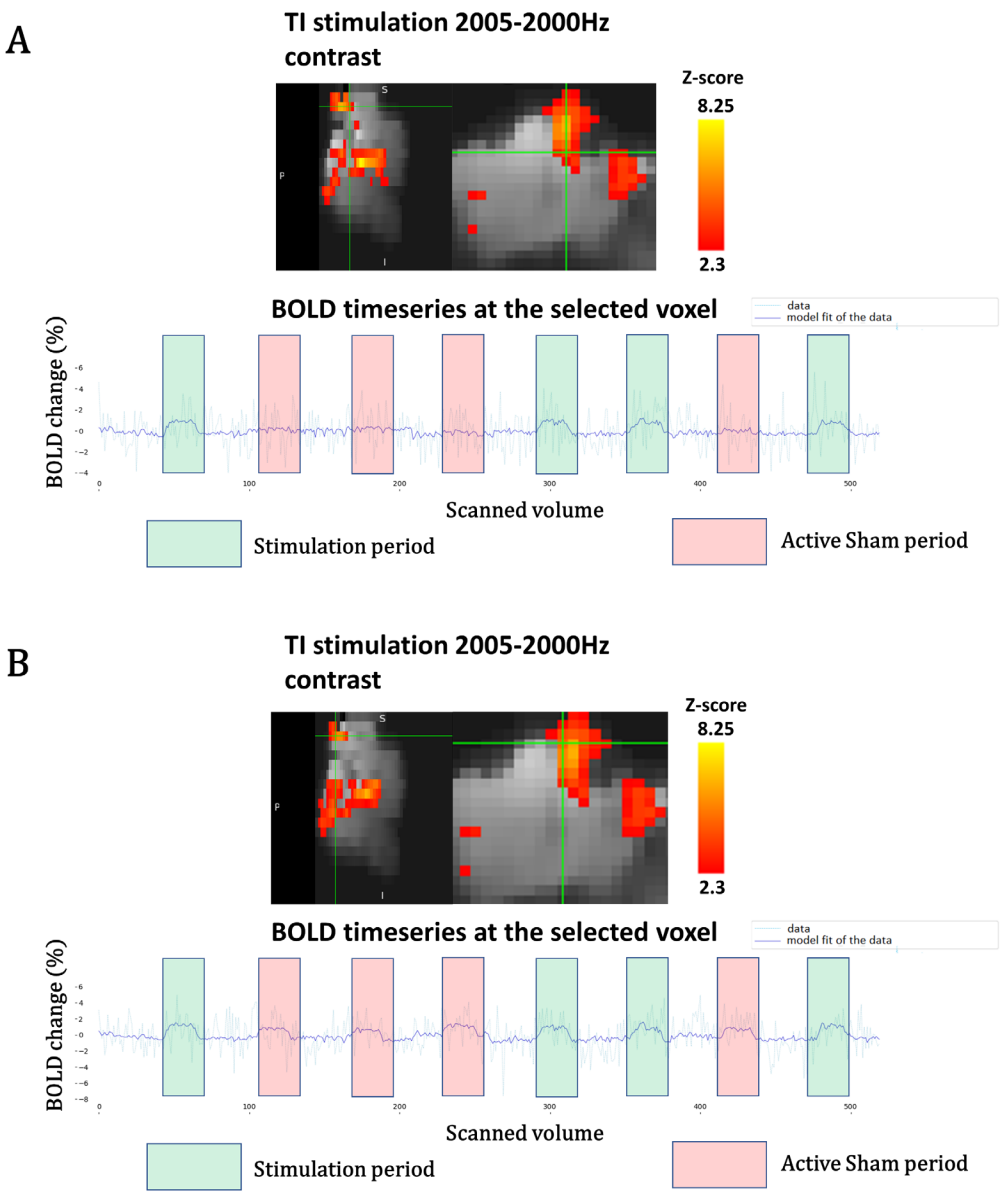

Figure S8. Dual nature of the off-target activation for Tripole TI-fMIR. Single animal

TI stimulation contrasts and BOLD timeseries at two different off-target voxels for a single fMRI session during TI tripole stimulation. Stimulation amplitude was 700 µA. Heatmap represents the results of general linear model analysis as z-scores.

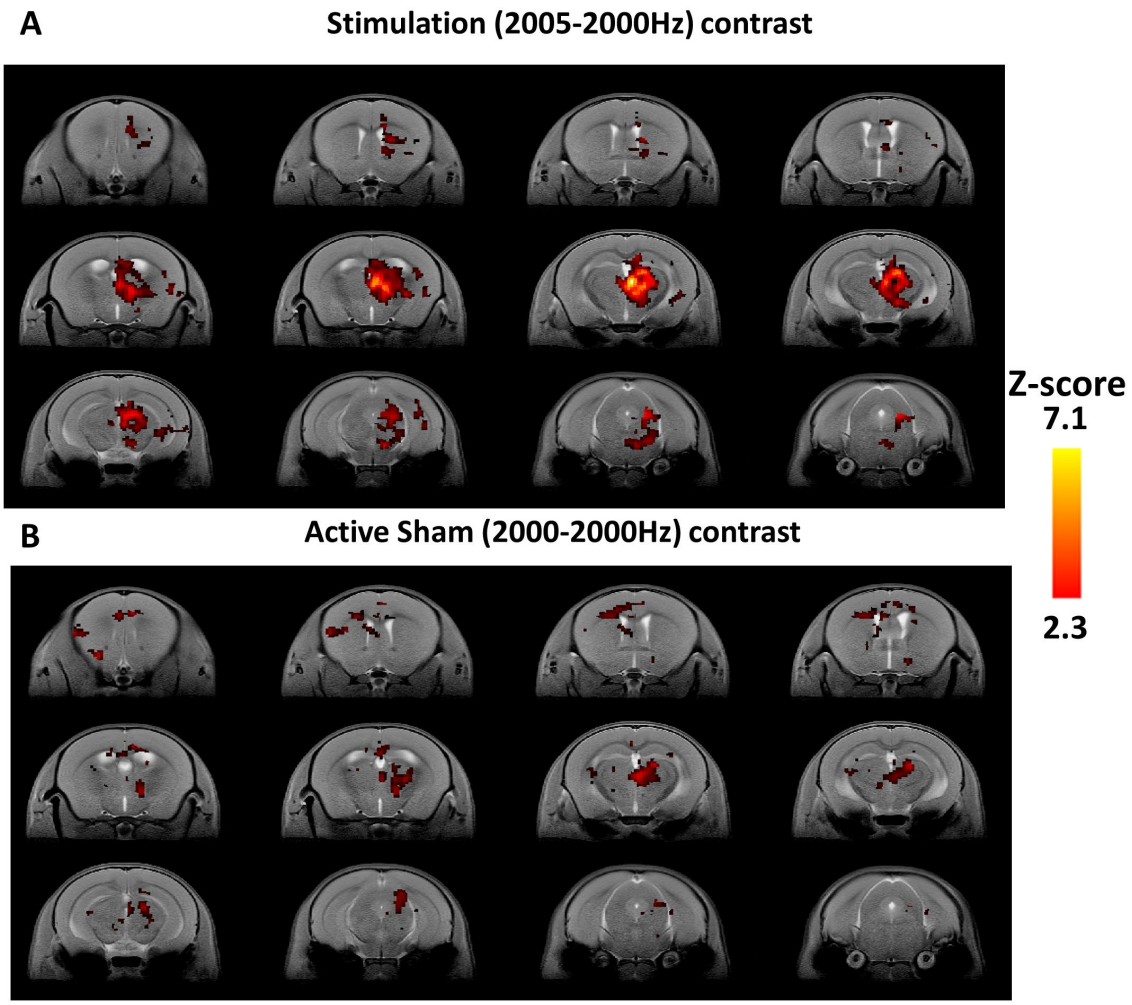

Figure S9. TI stimulation and Active Sham contrasts for Tripole TI-fMRI. Group level

A: TI stimulation contrast for front tripole design **B:** Active Sham contrast for front tripole design. Stimulation amplitude was 700 µA. Heatmap represents the results of general linear model analysis as z-scores at the group level (n=4).

Methods

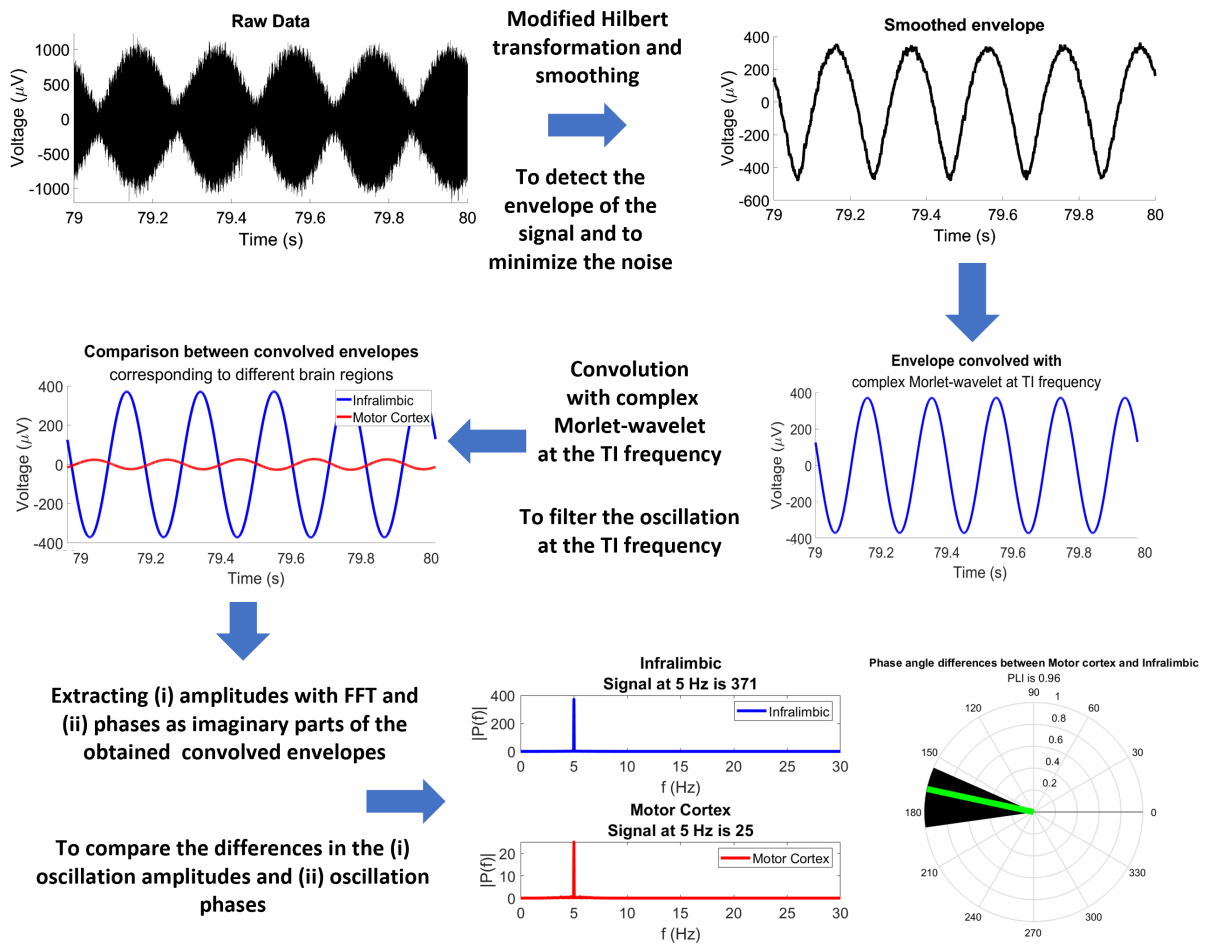

Figure S10. Post-processing steps of LFPs.

Processing pipeline of the electrophysiological recording obtained from each individual brain areas to get the signal filtered at TI frequency (e.g., 5 Hz). Outline of the filtered signal comparison between two different brain areas (e.g. Infralimbic and Motor cortices) is also shown in the bottom panel.

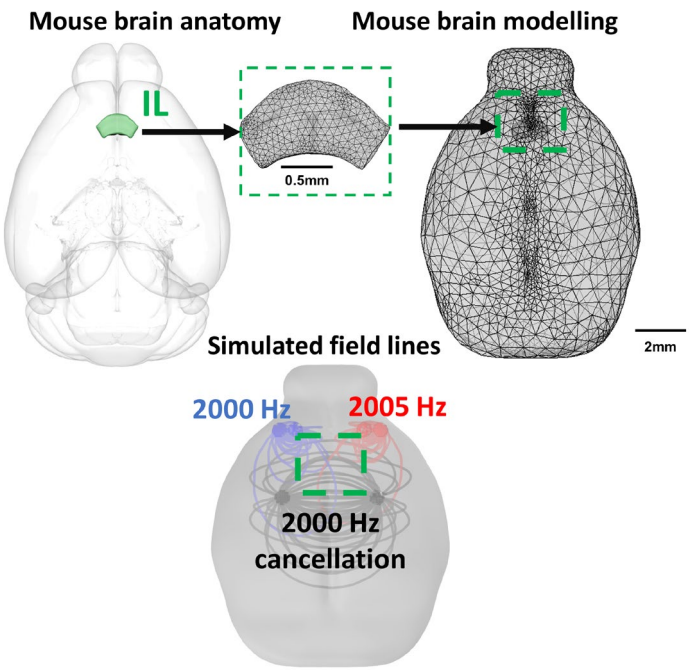

Figure S11. Modelling parameters for FEM, meshing.
Figure outlines the location of IL area in the mouse brain model and outlines the size parameters used for FEM meshing. The bottom scheme outlines the modeled field lines for dipole stimulation 2000Hz(blue) and 2005Hz(red), as well as for 2000 Hz(black) cancellation field.

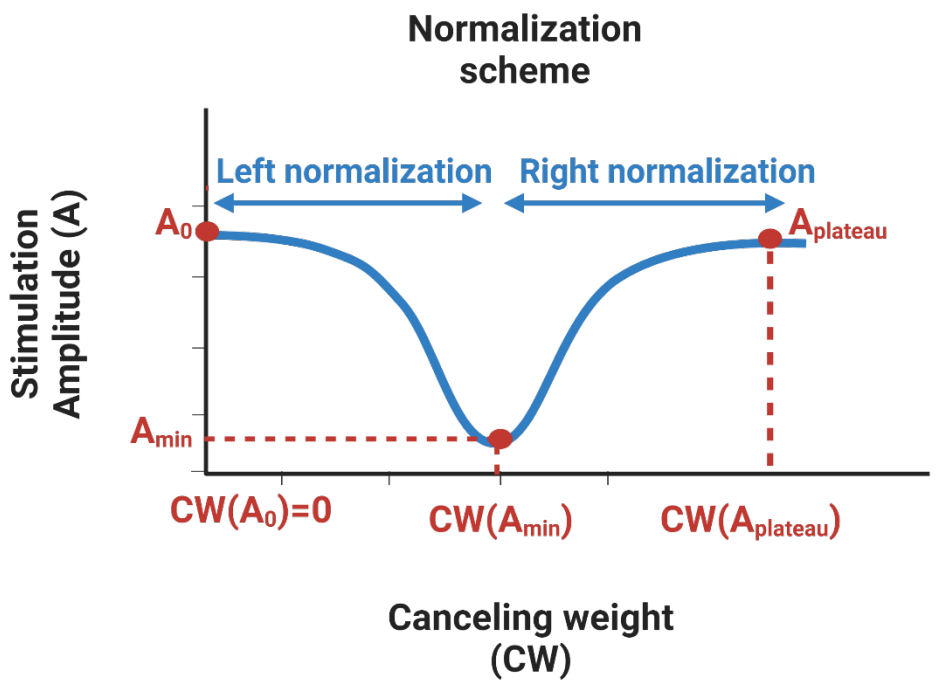

Figure S12. Normalization scheme.

Scheme features the reference points used in the normalization of the cancellation curve at equations 5-8. A_0, A_{plateu} and A_{min} refer to the Stimulation amplitudes at the corresponding canceling weights. Cancelling weight at A_0 is 0 and corresponds to the dipole configuration.

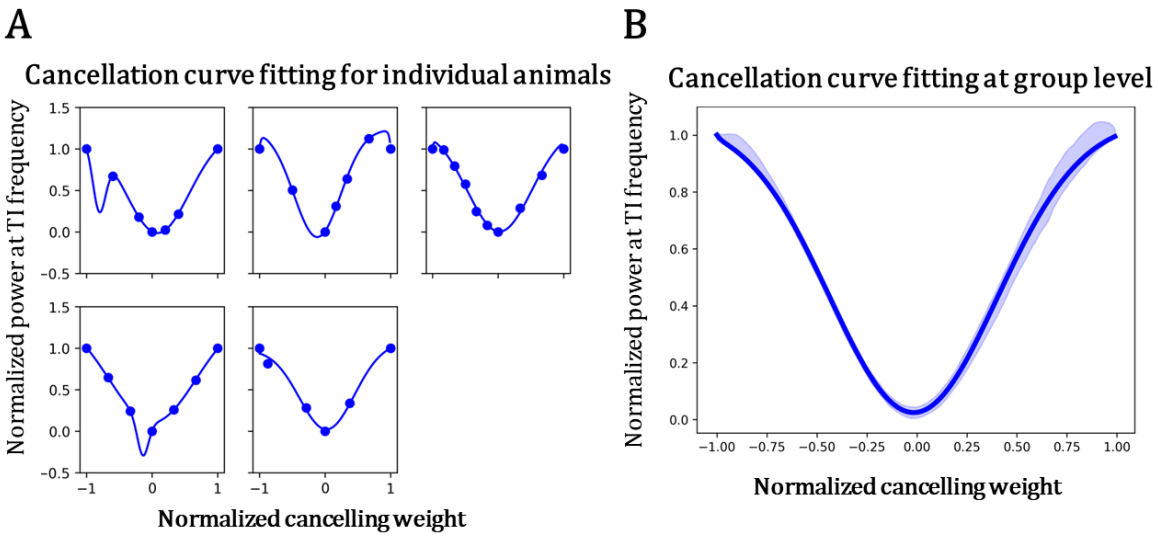

Figure S13. TI cancellation with a chronic implant.

A: Fitted cancellation curves for individual animals (n=5). **B:** Fitted cancellation curve at group level. Solid line represents the fitted model and shaded area depicts bootstrapped confidence interval (Q1 and Q3 percentiles).

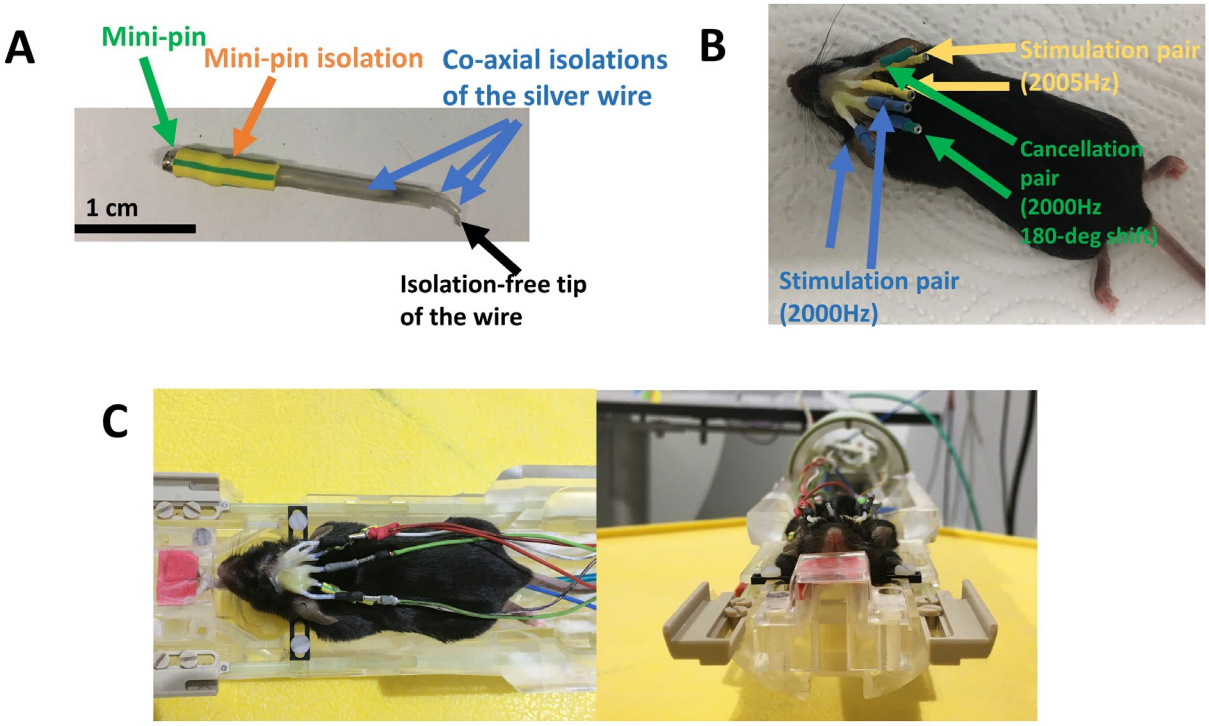

Figure S14. Chronic implant design.

A: Custom made electrodes used for the chronic implant **B:** Animal with the implant after the surgery. **C:** Animal with the implant during the fMRI session. Different animals are shown and, therefore, colors of electrode tips are different.

Contributions:

VZ and RP acquired funding and conceived the project. IS, VZ, FM and AW designed Ephys experiments and drafted data analysis concepts. IS, VZ and MM designed TI-fMRI experiments. IS performed Ephys experiments and corresponding data analysis. IS, DK and MM performed TI-fMRI experiments. IS and VZ conducted fMRI data analysis. VB performed computational modelling for dipole configuration with Sim4Life. FM and IS performed computational modelling for tripole configuration with COMSOL. IS and VZ wrote the manuscript and integrated corrections from all other authors. All authors contributed to the article and approved the submitted version.

Acknowledgements:

This work was supported by an ETH Grant (ETH-25 18-2) to R.P. and V.Z., by a Swiss National Science Foundation (SNSF) ECCELLENZA (PCEFP3_203005) to V.Z., and by a European Research Council (ERC) starting grant (ENTRAINER) to R.P. This project has received funding from the European Research Council (ERC) under the European Union's Horizon 2020 research and innovation program (grant agreement No. 758604). We thank Esra Neufeld and Antonino Cassara for their technical support with Sim4Life. We also thank Marius Moisa, Christopher Lewis, Friedhelm Hummel and Nicole Wenderoth for the important discussions and their support with the hardware.

References

Acerbo, E., Jegou, A., Luff, C., Dzialecka, P., Botzanowski, B., Missey, F., . . . Williamson, A. (2022). Focal non-invasive deep-brain stimulation with temporal interference for the suppression of epileptic biomarkers. *Front Neurosci, 16*, 945221. doi:10.3389/fnins.2022.945221

Alexander, M. L., Alagapan, S., Lugo, C. E., Mellin, J. M., Lustenberger, C., Rubinow, D. R., & Frohlich, F. (2019). Double-blind, randomized pilot clinical trial targeting alpha oscillations with transcranial alternating current stimulation (tACS) for the treatment of major depressive disorder (MDD). *Translational Psychiatry, 9*. doi:ARTN 106

10.1038/s41398-019-0439-0

Beliaeva, V., Savvateev, I., Zerbi, V., & Polania, R. (2021). Toward integrative approaches to study the causal role of neural oscillations via transcranial electrical stimulation. *Nat Commun, 12*(1), 2243. doi:10.1038/s41467-021-22468-7

Benjamini, Y., Krieger, A. M., & Yekutieli, D. (2006). Adaptive linear step-up procedures that control the false discovery rate. *Biometrika, 93*(3), 491-507. doi:DOI 10.1093/biomet/93.3.491

Botzanowski, B., Acerbo, E., Lehmann, S., Kearsley, S. L., Steiner, M., Neufeld, E., . . . Williamson, A. (2023). Controlling focality and intensity of non-invasive deep brain stimulation using multipolar temporal interference in non-human primates and rodents. *bioRxiv*, 2023.2009.2005.556444. doi:10.1101/2023.09.05.556444

Botzanowski, B., Donahue, M. J., Ejneby, M. S., Gallina, A. L., Ngom, I., Missey, F., . . . Williamson, A. (2022). Noninvasive Stimulation of Peripheral Nerves using Temporally-Interfering Electrical Fields. *Advanced Healthcare Materials, 11*(17). doi:ARTN 2200075

10.1002/adhm.202200075

Brown, M. B., & Forsythe, A. B. (1974). Robust Tests for the Equality of Variances. *Journal of the American Statistical Association, 69*(346), 364-367. doi:10.2307/2285659

Budde, R. B., Williams, M. T., & Irazoqui, P. P. (2023). Temporal interference current stimulation in peripheral nerves is not driven by envelope extraction. *J Neural Eng, 20*(2). doi:10.1088/1741-2552/acc6f1

Cao, J., & Grover, P. (2020). STIMULUS: Noninvasive Dynamic Patterns of Neurostimulation Using Spatio-Temporal Interference. *IEEE Trans Biomed Eng, 67*(3), 726-737. doi:10.1109/TBME.2019.2919912

Carmona-Barron, V. G., Fernandez Del Campo, I. S., Delgado-Garcia, J. M., De la Fuente, A. J., Lopez, I. P., & Merchan, M. A. (2023). Comparing the effects of transcranial alternating current and temporal interference (tTIS) electric stimulation through whole-brain mapping of c-Fos immunoreactivity. *Front Neuroanat, 17*, 1128193. doi:10.3389/fnana.2023.1128193

Cassarà, A., Newton, T., Zhuang, K., Regel, S., Achermann, P., Kuster, N., & Neufeld, E. (2022). Safety Recommendations for Temporal Interference Stimulation in the Brain. *bioRxiv*, 2022.2012.2015.520077. doi:10.1101/2022.12.15.520077

Cohen, M. X. (2015). Effects of time lag and frequency matching on phase-based connectivity. *J Neurosci Methods, 250*, 137-146. doi:10.1016/j.jneumeth.2014.09.005

Cohen, M. X. (2019). A better way to define and describe Morlet wavelets for time-frequency analysis. *NeuroImage, 199*, 81-86. doi:10.1016/j.neuroimage.2019.05.048

Collavini, S., Fernandez-Corazza, M., Oddo, S., Princich, J. P., Kochen, S., & Muravchik, C. H. (2021). Improvements on spatial coverage and focality of deep brain stimulation in pre-surgical epilepsy mapping. *Journal of Neural Engineering, 18*(4). doi:ARTN 046004

10.1088/1741-2552/abe5b9

Dandekar, M. P., Fenoy, A. J., Carvalho, A. F., Soares, J. C., & Quevedo, J. (2018). Deep brain stimulation for treatment-resistant depression: an integrative review of preclinical and

clinical findings and translational implications. *Mol Psychiatry, 23*(5), 1094-1112. doi:10.1038/mp.2018.2

Friedman, M. (1939). The use of ranks to avoid the assumption of normality implicit in the analysis of variance, (vol 32, pg 675, 1937). *Journal of the American Statistical Association, 34*(205), 109-109. doi:Doi 10.2307/2279169

Frohlich, F., & Riddle, J. (2021). Conducting double-blind placebo-controlled clinical trials of transcranial alternating current stimulation (tACS). *Translational Psychiatry, 11*(1), 284. doi:10.1038/s41398-021-01391-x

Goats, G. C. (1990). Interferential current therapy. *Br J Sports Med, 24*(2), 87-92. doi:10.1136/bjsm.24.2.87

Grimm, C., Wenderoth, N., & Zerbi, V. (2022). An optimized protocol for assessing changes in mouse whole-brain activity using opto-fMRI. *STAR Protoc, 3*(4), 101761. doi:10.1016/j.xpro.2022.101761

Grossman, N., Bono, D., Dedic, N., Kodandaramaiah, S. B., Rudenko, A., Suk, H. J., . . . Boyden, E. S. (2017). Noninvasive Deep Brain Stimulation via Temporally Interfering Electric Fields. *Cell, 169*(6), 1029-1041 e1016. doi:10.1016/j.cell.2017.05.024

Grover, S., Nguyen, J. A., Viswanathan, V., & Reinhart, R. M. G. (2021). High-frequency neuromodulation improves obsessive–compulsive behavior. *Nature Medicine, 27*(2), 232-238. doi:10.1038/s41591-020-01173-w

Han, Z., Chen, W., Chen, X., Zhang, K., Tong, C., Zhang, X., . . . Liang, Z. (2019). Awake and behaving mouse fMRI during Go/No-Go task. *NeuroImage, 188*, 733-742. doi:10.1016/j.neuroimage.2019.01.002

Hasgall, P. A., Di Gennaro, F., Baumgartner, C., Neufeld, E., Lloyd, B., Gosselin, M. C., . . . Kuster, N. (2022). IT' IS Database for thermal and electromagnetic parameters of biological tissues. *IT' IS Foundation, Version 4.1*. doi:DOI: 10.13099/VIP21000-04-1.

Krack, P., Hariz, M. I., Baunez, C., Guridi, J., & Obese, J. A. (2010). Deep brain stimulation: from neurology to psychiatry? *Trends in Neurosciences, 33*(10), 474-484. doi:10.1016/j.tins.2010.07.002

Kruskal, W. H., & Wallis, W. A. (1952). Use of Ranks in One-Criterion Variance Analysis. *Journal of the American Statistical Association, 47*(260), 583-621. doi:10.2307/2280779

Le Merre, P., Ahrlund-Richter, S., & Carlen, M. (2021). The mouse prefrontal cortex: Unity in diversity. *Neuron, 109*(12), 1925-1944. doi:10.1016/j.neuron.2021.03.035

Lee, J., Park, E., Kang, W., Kim, Y., Lee, K. S., & Park, S. M. (2021). An Efficient Noninvasive Neuromodulation Modality for Overactive Bladder Using Time Interfering Current Method. *Ieee Transactions on Biomedical Engineering, 68*(1), 214-224. doi:10.1109/Tbme.2020.2995841

Lee, M., Kim, D., Shin, H. S., Sung, H. G., & Choi, J. H. (2011). High-density EEG recordings of the freely moving mice using polyimide-based microelectrode. *J Vis Exp*(47). doi:10.3791/2562

Lui, P. L. (1990). Passive Intermodulation Interference in Communication-Systems. *Electronics & Communication Engineering Journal, 2*(3), 109-118. doi:DOI 10.1049/ecej:19900029

Ma, R., Xia, X. Z., Zhang, W., Lu, Z., Wu, Q. Y., Cui, J. T., . . . Zhang, X. C. (2022). High Gamma and Beta Temporal Interference Stimulation in the Human Motor Cortex Improves Motor Functions. *Frontiers in Neuroscience, 15*. doi:ARTN 800436

10.3389/fnins.2021.800436

Mann, H. B., & Whitney, D. R. (1947). On a Test of Whether one of Two Random Variables is Stochastically Larger than the Other. *The Annals of Mathematical Statistics, 18*(1), 50-60. Retrieved from http://www.jstor.org/stable/2236101

Markicevic, M., Savvateev, I., Grimm, C., & Zerbi, V. (2021). Emerging imaging methods to study whole-brain function in rodent models. *Transl Psychiatry, 11*(1), 457. doi:10.1038/s41398-021-01575-5

Mayberg, H. S., Lozano, A. M., Voon, V., McNeely, H. E., Seminowicz, D., Hamani, C., . . . Kennedy, S. H. (2005). Deep brain stimulation for treatment-resistant depression. *Neuron, 45*(5), 651-660. doi:10.1016/j.neuron.2005.02.014

Mirzakhalili, E., Barra, B., Capogrosso, M., & Lempka, S. F. (2020). Biophysics of Temporal Interference Stimulation. *Cell Syst, 11*(6), 557-572 e555. doi:10.1016/j.cels.2020.10.004

Missey, F., Donahue, M. J., Weber, P., Ngom, I., Acerbo, E., Botzanowski, B., . . . Williamson, A. (2022). Laser-Driven Wireless Deep Brain Stimulation using Temporal Interference and Organic Electrolytic Photocapacitors. *Advanced Functional Materials, 32*(33). doi:ARTN 2200691

10.1002/adfm.202200691

Missey, F., Ejneby, M. S., Ngom, I., Donahue J. , M., Trajlinek, J., Acerbo, E., . . . Williamson, A. (2023). Obstructive Sleep Apnea Improves with Non-invasive Hypoglossal Nerve Stimulation using Temporal Interference. *bioRxiv*, 2023.2004.2006.535917. doi:10.1101/2023.04.06.535917

Missey, F., Rusina, E., Acerbo, E., Botzanowski, B., Trebuchon, A., Bartolomei, F., . . . Williamson, A. (2021). Orientation of Temporal Interference for Non-invasive Deep Brain Stimulation in Epilepsy. *Front Neurosci, 15*, 633988. doi:10.3389/fnins.2021.633988

Oh, S. W., Harris, J. A., Ng, L., Winslow, B., Cain, N., Mihalas, S., . . . Zeng, H. (2014). A mesoscale connectome of the mouse brain. *Nature, 508*(7495), 207-214. doi:10.1038/nature13186

Oliveria, S. F. (2018). The dark history of early deep brain stimulation. *The Lancet Neurology, 17*(9), 748. doi:https://doi.org/10.1016/S1474-4422(18)30237-0

Padoa-Schioppa, C., & Assad, J. A. (2006). Neurons in the orbitofrontal cortex encode economic value. *Nature, 441*(7090), 223-226. doi:10.1038/nature04676

Quade, D. (1979). Using Weighted Rankings in the Analysis of Complete Blocks with Additive Block Effects. *Journal of the American Statistical Association, 74*, 680-683.

Ramirez-Zamora, A., Giordano, J. J., Gunduz, A., Brown, P., Sanchez, J. C., Foote, K. D., . . . Okun, M. S. (2018). Evolving Applications, Technological Challenges and Future Opportunities in Neuromodulation: Proceedings of the Fifth Annual Deep Brain Stimulation Think Tank. *Frontiers in Neuroscience, 11*. doi:ARTN 734

10.3389/fnins.2017.00734

Schaeuble, D., & Myers, B. (2022). Cortical-Hypothalamic Integration of Autonomic and Endocrine Stress Responses. *Front Physiol, 13*, 820398. doi:10.3389/fphys.2022.820398

Schlegel, F., Sych, Y., Schroeter, A., Stobart, J., Weber, B., Helmchen, F., & Rudin, M. (2018). Fiber-optic implant for simultaneous fluorescence-based calcium recordings and BOLD fMRI in mice. *Nat Protoc, 13*(5), 840-855. doi:10.1038/nprot.2018.003

Schreglmann, S. R., Wang, D., Peach, R. L., Li, J., Zhang, X., Latorre, A., . . . Grossman, N. (2021). Non-invasive suppression of essential tremor via phase-locked disruption of its temporal coherence. *Nat Commun, 12*(1), 363. doi:10.1038/s41467-020-20581-7

Shapiro, S. S., & Wilk, M. B. (1965). An Analysis of Variance Test for Normality (Complete Samples). *Biometrika, 52*(3/4), 591-611. doi:10.2307/2333709

Song, S. X., Zhang, J. J., Tian, Y., Wang, L. P., & Wei, P. F. (2021). Temporal Interference Stimulation Regulates Eye Movements and Neural Activity in the Mice Superior Colliculus. *2021 43rd Annual International Conference of the Ieee Engineering in Medicine & Biology Society (Embc)*, 6231-6234. doi:10.1109/Embc46164.2021.9629968

Song, X., Zhao, X., Li, X., Liu, S., & Ming, D. (2021). Multi-channel transcranial temporally interfering stimulation (tTIS): application to living mice brain. *J Neural Eng, 18*(3). doi:10.1088/1741-2552/abd2c9

Stam, C. J., Nolte, G., & Daffertshofer, A. (2007). Phase lag index: assessment of functional connectivity from multi channel EEG and MEG with diminished bias from common sources. *Hum Brain Mapp, 28*(11), 1178-1193. doi:10.1002/hbm.20346

Student. (1908). The Probable Error of a Mean. *Biometrika, 6*(1), 1-25. doi:10.2307/2331554

Sullivan, C. R. P., Olsen, S., & Widge, A. S. (2021). Deep brain stimulation for psychiatric disorders: From focal brain targets to cognitive networks. *NeuroImage, 225*, 117515. doi:https://doi.org/10.1016/j.neuroimage.2020.117515

Violante, I. R., Alania, K., Cassarà, A., M., Neufeld, E., Acerbo, E., Carron, R., . . . Grossman, N. (2022). Non-invasive temporal interference electrical stimulation of the human hippocampus. *bioRxiv*, 2022.2009.2014.507625. doi:10.1101/2022.09.14.507625

Voroslakos, M., Takeuchi, Y., Brinyiczki, K., Zombori, T., Oliva, A., Fernandez-Ruiz, A., . . . Berenyi, A. (2018). Direct effects of transcranial electric stimulation on brain circuits in rats and humans. *Nat Commun, 9*(1), 483. doi:10.1038/s41467-018-02928-3

Wang, Q., Ding, S. L., Li, Y., Royall, J., Feng, D., Lesnar, P., . . . Ng, L. (2020). The Allen Mouse Brain Common Coordinate Framework: A 3D Reference Atlas. *Cell, 181*(4), 936-+. doi:10.1016/j.cell.2020.04.007

Welch, B. L. (1947). The Generalization of `Student's' Problem when Several Different Population Variances are Involved. *Biometrika, 34*(1/2), 28-35. doi:10.2307/2332510

Welch, B. L. (1951). On the Comparison of Several Mean Values: An Alternative Approach. *Biometrika, 38*(3/4), 330-336. doi:10.2307/2332579

Wessel, M. J., Beanato, E., Popa, T., Windel, F., Menoud, P., Beliaeva, V., . . . Hummel, F. C. (2021). Evidence for temporal interference (TI) stimulation effects on motor striatum. *Brain Stimulation: Basic, Translational, and Clinical Research in Neuromodulation, 14*(6), 1684. doi:10.1016/j.brs.2021.10.307

Wilcoxon, F. (1945). Individual Comparisons by Ranking Methods. *Biometrics Bulletin, 1*(6), 80-83. doi:Doi 10.2307/3001968

Williams, N. R., Bentzley, B. S., Hopkins, T., Pannu, J., Sahlem, G. L., Takacs, I., . . . Short, E. B. (2018). Optimization of epidural cortical stimulation for treatment-resistant depression. *Brain Stimulation, 11*(1), 239-240. doi:10.1016/j.brs.2017.09.001

Wu, L. Y., Liu, T., & Wang, J. (2021). Improving the Effect of Transcranial Alternating Current Stimulation (tACS): A Systematic Review. *Frontiers in Human Neuroscience, 15*. doi:ARTN 652393

10.3389/fnhum.2021.652393

Xue, M., Shi, W. T., Zhou, S. B., Li, Y. N., Wu, F. Y., Chen, Q. Y., . . . Zhuo, M. (2022). Mapping thalamic-anterior cingulate monosynaptic inputs in adult mice. *Mol Pain, 18*, 17448069221087034. doi:10.1177/17448069221087034

Zandvakili, A., Berlow, Y. A., Carpenter, L. L., & Philip, N. S. (2019). Transcranial Direct Current Stimulation in Psychiatry: What Psychiatrists Need to Know. *Focus (Am Psychiatr Publ), 17*(1), 44-49. doi:10.1176/appi.focus.20180029